Energy Conversion and Management: X 25 (2025) 100830

Contents lists available at ScienceDirect

Energy Conversion and Management: X

journal homepage: www.sciencedirect.com/journal/energy-conversion-and-management-x

The effect of Coriolis force on the coherent structures in the wake of a 5MW wind turbine

Felice Manganelli [a,*], Claudio Bernardi [a], Alessandro Giannotta [a], Stefano Leonardi [b], Stefania Cherubini [a], Pietro De Palma [a]

[a] Department of Mechanics, Mathematics and Management, Polytechnic University of Bari, Via Orabona 4, Bari, 70126, Italy
[b] Department of Mechanical Engineering, University of Texas at Dallas, 800 W Campbell Road, Richardson, 75080, TX, USA

ARTICLE INFO

Keywords:
Dynamic Mode Decomposition
Large Eddy Simulation
Wind veer

ABSTRACT

This study aims to investigate the effect of Coriolis acceleration on the coherent structures in the wake of the NREL-5MW wind turbine, using the Dynamic Mode Decomposition (DMD). The Coriolis acceleration induces an altitude-dependent lateral deviation of the incoming wind direction (veer), which can substantially affect the performance of wind turbines. Large eddy precursor simulations are carried out to generate turbulent inlet velocity profiles. The presence of a veer stretches the turbine wake and influences the dynamics of the coherent structures. We decompose the flow structures to extract a limited subset of relevant flow features that optimally approximate the original data sequence, using the Sparsity-Promoting (SP) version of the DMD algorithm to rank the most relevant modes. It is found that wind veer induces coherent structures with a spanwise velocity component of the same order of the streamwise one and oblique shape. Using proper orthogonal decomposition, we analyze the contribution of the coherent structures to the mean kinetic entrainment. We found that due to wind veer, shorter wavelength mode pairs contribute mostly to wake recovery. Finally, we derive a reduced order model using approximately 70 modes pairs, which reproduces the flow structure with 5%–7% error.

1. Introduction

According to the 2023 IRENA report, global installed renewable power capacity will need to triple from 3 382 GW by 2025 to 11 174 GW by 2030, with wind contributing around 32% [1]. To achieve the above target, it is essential to improve the efficiency of new turbines and wind farms, due to the necessity of reducing the use of land and sea. When it comes to modern wind turbine design, there is a noticeable trend towards increasing rotor diameters and hub heights to attain enhanced power output. In the case of onshore installations, a single turbine should be capable of producing 5–6 MW in the near term, with an average installed capacity of 2.6 MW in 2018, and a diameter of 160–170 m, whereas, for offshore systems, a single turbine with diameter of around 250 m and hub height of 150 m will produce 15 to 20 MW in the next 10 to 20 years [2].

With current turbine hubs of the order of 100 m and the expectation of even higher hubs in the future, it is crucial to understand how the blades operate within the Atmospheric Boundary Layer (ABL) [3]. Due to the presence of the ground, a velocity gradient is formed along the vertical direction and as the size of the turbine increases, the effects of this phenomenon have a greater influence on the blade loads [4]. Thus, for efficiently designing and optimizing the performance of a wind farm, it is necessary to accurately take into account the influence of the ABL, since its characteristics have a significant impact on the rotors, which in turn affects the dynamics of their wakes [5]. From a practical perspective, the wind direction with respect to the rotor and its turbulence intensity can affect the wake recovery rate and how the wake develops, in terms of velocity loss and direction. The higher the turbulence intensity level, the higher the wake recovery rate, according to numerical [6] and experimental data [7,8]. It has been demonstrated that turbulence significantly alters the wake structure and its recovery [9]. In particular, the wake generated by the turbine evolves more rapidly for high turbulence intensity and low integral time scale of the impinging flow. Moreover, as discussed in De Cillis et al. [10], the presence of turbulence in the flow investing the turbine induces low-frequency oscillations in the wake that are consistent with those of the upstream ABL and extend further in the far wake region. All these literature results thus suggest the necessity of integrating atmospheric turbulence into low-dimensional models of turbine wakes.

Another typical feature of the ABL, particularly relevant for large-rotor turbines, is the formation of an Ekman spiral that occurs within its surface layer due to the Coriolis acceleration induced by the Earth's

* Corresponding author.
E-mail address: f.manganelli@phd.poliba.it (F. Manganelli).

https://doi.org/10.1016/j.ecmx.2024.100830
Received 13 August 2024; Received in revised form 4 December 2024; Accepted 4 December 2024
Available online 25 December 2024

rotation. As a result, the wind direction changes with height. Consequently, the spanwise component of the wind, known as wind veer, becomes height-dependent. This phenomenon can affect the output of wind farms [11] and the recovery rate of the individual turbine wake [12]. The Gaussian wake model has been enhanced to incorporate wind veer considerations [13]. This revised model predicts the wake structure, characterized by skewness and shear, resulting from spanwise wind veer. The study in Ref. [13] has been conducted using Large-Eddy Simulations (LES), with an isolated turbine rotor modeled by the actuator disk approach. Further studies have been conducted to define the effect of yaw and veer on blade dynamics. This was achieved through the use of LES, which involved the modeling of the blades with an actuator line model [14] and an actuator disk model [15]. As demonstrated in the aforementioned papers, the incorporation of a more realistic approach, specifically the addition of geostrophic forcing, has revealed that wind veer exerts a notable influence on the outcome of simulations. The wake has an oblique spatial structure, an increased turbulent intensity, and is characterized by a deflection inducing the need for the turbines downstream to adapt to this deflected flow in terms of yaw misalignment. Finally, a modification of the reduced-order prediction models taking into account these effects is required.

Despite the dynamics of wind farms and isolated wind turbines in the presence of wind veer have been considered in several studies, the effect of the veer on the frequencies and wavelengths of the coherent flow structures in the wake of the turbines is still to be determined. Notably, the study and modelization of such coherent structures developing in the wake of wind turbines is particularly interesting for evaluating the interaction between turbines, especially within a wind farm, which is a key aspect of power generation. As discussed in Refs. [5,16], in wind farms wakes play a primary role, particularly when aiming at increasing the power density of a wind farm by reducing the distance between the turbines, which intensifies the interaction of the downstream turbines with the wakes upstream [17]. Thus, for easily evaluating the potential effect of the turbine's wake impacting on the downstream ones, it is crucial to study, characterize, and model in a computationally cheap way the wake dynamics in realistic conditions, such as in the presence of turbulent fluctuations, sheared inflow, wind veer, etc. Among the possible methods for creating accurate reduced-order models of the wind turbine's flow field, Proper Orthogonal Decomposition [18] and Dynamic Mode Decomposition [19] are the most relevant. Both methods have already been used for reconstructing the flow field [10,20–23] in the wake of wind turbines, although DMD has the advantage of being based on modes having a given frequency and amplitude instead of a multi-frequency amplitude function as POD ones. Being characterized by a single time–frequency, the DMD modes can be sorted by their spectral contribution and spatial growth rate, which is particularly interesting for the design of a wind farm layout, where determining the frequencies involved in the dynamic load acting on downstream turbines is paramount. Moreover, variants of the former decomposition [24] allowing a penalized minimization of the error ensuring the selection of a limited subset of modes have been developed, which are particularly adequate for the construction of reduced-order models of the flow field. However, DMD modes are non-orthogonal, so they cannot be used for evaluating global flow variables (such as, for instance, the mean kinetic energy entrainment) through linear superposition of the contribution of the different modes, such as it is usually done with POD modes, which constitute an orthonormal basis.

In this framework, the main contribution of the present study is twofold. The first is to evaluate the effects of Coriolis acceleration in a turbulent neutral ABL on the coherent structures in an NREL-5MW reference wind turbine's wake comparing them with those observed in the absence of wind veer. The second is to construct a reduced-order model of the wake of the considered turbine taking into account the Coriolis effect, using a restricted set of Dynamic modes. These analyses are conducted using Sparsity Promoting Dynamic Mode Decomposition (SP-DMD) [24] to identify the most relevant dynamically coherent structures within the turbine wake. Rowley et al. [25] developed the theory of DMD to compute the Koopman expansion of a sequence of flow-field snapshots. An updated version of this theory was created by Schmid [19]. The DMD approach is based on the identification of eigenvalues and associated eigenvectors associated with a linear approximation of a non-linear dynamical system embedded within the data sequence. This methodology has recently been utilized for the construction of reduced order model (ROM) formulations for wind turbine flow simulations, as detailed in Ref. [23]. The use of DMD enables the analysis of time-resolved data, including a sequence of snapshots obtained from either computational simulations or experimental investigations. This data is employed to identify the more dynamically relevant coherent structures, known as DMD modes, which characterize the flow dynamics. These modes have a single-time frequency and a complex spatial distribution. This is of particular interest in the context of wind farm layout design, as it enables the identification of the most significant frequencies involved in the dynamic load acting over downstream turbines. In the context of wind energy, it would be beneficial to ascertain which of these mono-frequential modes retain a greater energy contribution. Sun et al. [26] computed the dynamics of an unsteady flow over a two-blade wind turbine through LES and investigated the wake flow dynamics using the DMD method. Concerning the interaction of turbines, only a few modes have been found to bear significant importance. This allows for the possibility of simplified models for optimization purposes [27]. However, it is necessary to use selection criteria for the realization of a dynamically relevant subset of modes, otherwise one could end up with inaccurate ROMs. In the present work, the Sparsity Promoting (SP) algorithm [24] is used to rank the most relevant DMD modes, extracted by a sequence of flow-field snapshots of LES. The actuator line method is employed to simulate the rotor, whereas the tower and nacelle are modeled through the Immersed boundary method [10,28]. The NREL-5MW wind turbine has been chosen as a realistic reference test case for a MW-scale wind turbine since both the details of the turbine's geometry and a complete data set are extensively documented in literature [29]. Two different scenarios of wind impinging the turbine have been chosen in this study: a neutral ABL considering the presence of Coriolis acceleration and one without any wind veer.

2. Methodologies

In this section, the numerical method employed to discretize and to solve the Navier–Stokes equations is described. Furthermore, the actuator line model for the turbine rotor is briefly recalled. Then we discuss the techniques employed to analyze the three-dimensional numerical data set generated by the numerical simulations. In particular, we firstly describe the Proper Orthogonal Decomposition (POD) and the Dynamic Mode Decomposition (DMD) methods, which allow one to extract from the flow the more energetically and dynamically relevant coherent structures, respectively. Then, we discuss the sparsity promoting DMD algorithm, which is employed to limit the number of relevant DMD modes in order to construct an efficient and accurate reduced order model of the flow. Finally, we provide the procedure to perform the analysis of the mean kinetic energy entrainment in the wake of the turbine.

2.1. Large Eddy Simulations

In the present work the Large Eddy Simulation (LES) approach is used to compute the dynamics of the wake behind the NREL 5-MW wind turbine in two different inflow conditions. The simulations are carried out by solving the Navier–Stokes equations, as follows:

$$\frac{\partial u_i}{\partial t}+\frac{\partial u_i u_j}{\partial x_j}=-\frac{\partial p}{\partial x_i}+\frac{1}{Re}\frac{\partial^2 u_i}{\partial x_j \partial x_j}-\frac{\partial \tau_{ij}}{\partial x_j}+f_c e_{i2j}(u_j-u_{gj})+F_{PI,i}+F_i, \quad (1)$$

$$\frac{\partial u_i}{\partial x_i} = 0, \tag{2}$$

where u_i is the filtered non-dimensional velocity, whose components are indicated with $i, j \in \{1, 2, 3\}$ referring to the streamwise (x), wall-normal (y) and spanwise (z) non-dimensional directions, respectively; τ_{ij} is the modeled sub-grid scale stress tensor; f_c is the Coriolis frequency; u_{g_j} is the imposed geostrophic velocity component; F_i a forcing term representing the aerodynamic forces per unit volume exerted by the turbine blades on the fluid modeled by the actuator line method. The pressure p and the isotropic part of the sub-grid scale stress tensor $\frac{1}{3}\tau_{ii}$ are combined to represent the modified filtered pressure p^*. The anisotropic part τ^r_{ij} is modeled using the Smagorinsky model [30], to capture the effects of small-scale structures on the filtered flow. The Smagorinsky model has been widely used for similar wind turbine flows (for instance, see Martínez-Tossas et al. [31]). The effect of different subgrid-scale models on the filtered flow have been compared by Ciri et al. [32,33] on the Blind test 1 and 4 [34] and by Sarlak et al. [35], indicating a weak dependence of the wake dynamics. Therefore, in the present paper we have chosen to employ the Smagorinsky model because already validated in these previous studies. A constant $C_s = 0.09$ is employed and this choice is justified by the fact that this value has been highly used for simulations of flows similar to those considered in this study (see [31–33]). The term $F_{PI,i}$ is the Proportional–Integral (PI) wind controller correction on the ABL, whose purpose is to move the Ekman profile, to have a zero spanwise velocity component at hub height. The geostrophic wind angle is adjusted by imposing the following source terms throughout the domain:

$$\begin{cases} F_{PI,1} = +\omega_{PI} u_3 \\ F_{PI,2} = 0 \\ F_{PI,3} = -\omega_{PI} u_1 \end{cases} \tag{3}$$

where ω_{PI} is the control action whose values will be discussed later. The action of these forces results in a counter-clockwise rotation of the flow field around the vertical axis of the angle:

$$\theta = \tan^{-1}(< u_3 > / < u_1 >) \tag{4}$$

where $< u_3 >$ and $< u_1 >$ represent the horizontally averaged velocity components along the spanwise and streamwise directions, respectively. The PI controller aims at reducing the difference between the actual flow angle θ respecting a chosen desired value $\theta_{desired}$, by adapting the values of the streamwise and spanwise components of the geostrophic velocity, u_{g1} and u_{g3}. In consideration of the nature of the controller, the control action can be succinctly described as follows:

$$\omega_{PI}(t) = K_P\, e(t) + K_I \int e(t)\, dt \tag{5}$$

where $e(t)$ is the error, calculated as the difference between $\theta_{desired}$ and θ at hub-height. Since the controller aims to avoid yaw misalignment, we choose $\theta_{desired} = 0$ and we compute the averaged velocities $< u_3 >, < u_1 >$ at hub height. The geostrophic velocity magnitude $G = (u^2_{g1} + u^2_{g3})^{1/2}$ is kept constant while the controller updates the streamwise and spanwise components, u_{g1} and u_{g3}. Upon reaching a steady-state condition having a value of θ lower than a threshold value, the controller switches off.

The Reynolds number $Re = \frac{U_\infty D}{\nu}$ is defined as a function of the main flow variables referred to the reference wind turbine, such that U_∞ is the free-stream velocity at the hub height, D is the rotor diameter, and ν the kinematic viscosity of the fluid. An in-house code developed at UT Dallas, known as UTD-WF (see [36]) is used to conduct the simulations discussed in this paper. The code has been extensively validated against numerical results provided in Ref. [37] regarding the NREL 5MW reference turbine as well as experimental wind tunnel data [38]. A second-order accurate centered finite difference scheme on a Cartesian grid is used to discretize the governing equations. Whereas, the time integration is carried out employing a hybrid low-storage third-order accurate Runge–Kutta scheme [39].

The aerodynamic forces, computed using the coefficient of lift, C_L, and drag, C_D, of the rotor blades are imposed through the actuator line method [40]. The rotor blades are approximated as rotating rigid lines that are divided into discrete segments. For each element, the lift and drag forces are estimated as:

$$F_L = \frac{1}{2}\rho u^2_{rel} C_L(\alpha) c F, \tag{6}$$

$$F_D = \frac{1}{2}\rho u^2_{rel} C_D(\alpha) c F, \tag{7}$$

where ρ is the fluid density, c is the chord, u_{rel} is the relative inflow velocity, α is the angle of attack, F is the modified Prandtl correction factor, which considers the aerodynamic effect of the tip and root vortices. To distribute the aerodynamic forces across an area perpendicular to each actuator line, F_D and F_L are multiplied for a Gaussian distribution kernel.

The immersed boundary method is employed to describe the tower and nacelle. This allows for reducing the computational cost of the LES and avoiding the use of a body-fitted grid [10,22,41].

2.2. Dynamic Mode Decomposition

Dynamical Mode Decomposition [19,25] is a mathematical technique used to analyze datasets providing the evolution of a dynamical system. In the field of fluid dynamics, the approach assumes that the system's evolution can be approximated by a linear transformation between successive snapshots coming from simulations or experiments of a given flow. This allows for the identification of dynamically relevant flow structures, referred to as dynamic modes, by analyzing the inherent patterns in the simulated data. In this study, snapshots of the flow field are acquired from numerical simulations for data collection. Each snapshot, represented as $q^i \in \mathbb{R}^N$, is collected at a uniform sampling rate. The size of the snapshots (N) is determined by multiplying the number of observables (O), which in this case are the three components of the velocity, by the number of measurement points (S), which is the number of grid points selected for the DMD analysis (see Section 2.3). The relationship between two consecutive snapshots, assuming a linear time-invariant mapping A and M snapshots, can be expressed as follows:

$$q_{i+1} = A q_i, \qquad i = \{0, \dots, M-1\}. \tag{8}$$

Thus, defining the snapshot matrix

$$Q_i = [q_i\ q_{i+1}\ \cdots\ q_{M-1+i}], \tag{9}$$

and combining (8) and (9), one has:

$$Q_i = A Q_{i-1}. \tag{10}$$

To ensure that the computational procedure is both robust and affordable, a low-dimensional representation of A is required. To achieve this, we project the snapshot matrix Q_0 onto a low-rank orthogonal basis using a singular value decomposition (SVD) technique $Q_0 = U \Sigma V^T$, known as Proper Orthogonal Decomposition (POD), where U contains the POD modes u_i in its columns, while Σ is a diagonal matrix filled by non-zero singular values in its diagonal, which describe the energy contained in each POD mode. The optimal rank-r approximation of Q_0, obtained after selecting a POD subspace of dimension r, is defined as:

$$\tilde{Q}_0 = \tilde{U} \tilde{\Sigma} \tilde{V}^T, \tag{11}$$

where $\tilde{U}$ and $\tilde{V}$ denote the first r leading columns of U and V and $\tilde{\Sigma}$ contains the leading $r \times r$ sub-block of Σ (*i.e.*, the most energetic singular values, s_k, of the POD). On this reduced basis, a POD-projected similar matrix $\tilde{A}$ is constructed, corresponding to the solution of the following optimization problem,

$$\min_A \| Q_1 - \tilde{U} \tilde{A} \tilde{\Sigma} \tilde{V}^T \|^2_F, \tag{12}$$

where $\tilde{A}$ is defined by the similarity transformation

$$A = \tilde{U} \tilde{A} \tilde{U}^T, \tag{13}$$

and thus can be obtained as:

$$\tilde{A} = \tilde{U}^T \tilde{Q}_1 \tilde{V} \tilde{\Sigma}^{-1}. \tag{14}$$

To extract the dynamic modes, the eigendecomposition of the similar matrix is firstly computed as:

$$\tilde{A} = \underbrace{[y_1 \ \dots \ y_r]}_{Y} \underbrace{\begin{bmatrix} \mu_1 & 0 & \cdots & 0 \\ 0 & \mu_2 & \cdots & 0 \\ \vdots & \vdots & \ddots & \vdots \\ 0 & 0 & \cdots & \mu_r \end{bmatrix}}_{D_\mu} \underbrace{\begin{bmatrix} z_1^* \\ z_2^* \\ \vdots \\ z_r^* \end{bmatrix}}_{Z^*} \tag{15}$$

where y_k and z_k^* are the left and right eigenvectors of $\tilde{A}$, respectively, normalized as $y_k^* y_k = 1$ and $z_k^* y_j = \delta_{kj}$, while the μ_k represent the r eigenvalues of the similar matrix. The DMD modes are then computed as:

$$\phi_k = \tilde{U} y_k, \tag{16}$$

and their associated complex frequency can be recovered by the associated values of μ_k, as will be detailed in Section 4.1.2.

To allow a reconstruction of the flow field, each DMD mode should also be associated with a given amplitude. For recovering the associated amplitude, we first notice that the flow field in the POD subspace for the ith snapshot can be reconstructed as follows:

$$x_i = \tilde{A}^i x_0 = W D_\mu^i Z^T x_0 = \sum_{k=1}^{r} y_k \mu_k^i z_k^* x_0 = \sum_{k=1}^{r} y_k \mu_k^i \alpha_k, \tag{17}$$

which can be reported in the non-projected space as:

$$q_i \approx \tilde{U} x_i = \sum_{k=1}^{r} \tilde{u}_k y_k \mu_k^i \alpha_k = \sum_{k=1}^{r} \phi_k \mu_k^i \alpha_k \tag{18}$$

where α_k is the amplitude of the kth DMD mode. Therefore, Q_0 can be defined in matrix form:

$$\underbrace{[q_0 \ \dots \ q_{M-1}]}_{Q_0} \approx \underbrace{[\phi_1 \ \dots \ \phi_r]}_{\Phi} \times \underbrace{\begin{bmatrix} \alpha_1 & 0 & \cdots & 0 \\ 0 & \alpha_2 & \cdots & 0 \\ \vdots & \vdots & \ddots & \vdots \\ 0 & 0 & \cdots & \alpha_r \end{bmatrix}}_{D_\alpha} \underbrace{\begin{bmatrix} 1 & \mu_1 & \dots & \mu_1^{M-1} \\ 1 & \mu_2 & \dots & \mu_2^{M-1} \\ \vdots & \vdots & \ddots & \vdots \\ 1 & \mu_r & \dots & \mu_r^{M-1} \end{bmatrix}}_{V_{and}} \tag{19}$$

where V_{and} is the Vandermonde matrix, which contains the r eigenvalues of $\tilde{A}$ for each sample. The amplitudes α_k are determined through minimization of the approximation, defined by the following Frobenius norm:

$$\min_{\alpha_i} \ J(\alpha_i) = \| Q_0 - \Phi D_{\alpha_i} V_{and} \|_F^2 \tag{20}$$

or by more elaborate minimizations as discussed in the following.

2.3. Sparsity promoting Dynamic Mode Decomposition

ROMs usually aim at reconstructing with sufficient accuracy the flow field evolution with a rather small number of modes. However, the minimization problem in Eq. (20) neglects the number of modes selected for the reconstruction. Whereas, a concise representation of the system's behavior can be achieved using a different error minimization strategy, penalizing the number of modes used for the reconstruction. In this study, the sparsity of the extracted dynamic modes is ensured by using the SP-DMD proposed by Jovanović et al. [24]. Through a constrained error minimization penalizing the non-zero amplitudes associated to the DMD modes, a limited number of modes (along with their optimized amplitude values) are selected for the reconstruction of the dataset. This goal is achieved through the use of a modified objective function:

$$\min_{\alpha} \quad J(\alpha) + \gamma \sum_{i=1}^{r} |\alpha_i|, \tag{21}$$

where γ is a positive regularization parameter chosen by the user. Sparser solutions are obtained for larger values of γ. The convex optimization problem in Eq. (21) is solved using the Alternating Direction Method of Multipliers.

2.4. Mean kinetic energy equation

In order to study the turbulent energy fluxes in the wake of the wind turbine, we employ the transport equation for the turbulent mean kinetic energy. In fact, an increase in the intensity of the turbulence acting on the turbine is associated with an increase in the wake recovery rate [42–44]. This is justified by the diffusion generated by the turbulence fluctuations, which improves the transport of the mean kinetic energy within the wake.

The effect of the coherent structures within the wake on its recovery is evaluated by considering the contribution of each POD mode to wake recovery. In the present analysis, POD modes are used instead of DMD ones for two main reasons. Firstly, POD modes represent the most energetic structures within the flow, and are thus well suited for evaluating the energy exchange among the modes, the mean flow, and/or the turbulent fluctuations. Then, POD modes constitute an orthonormal basis, allowing an evaluation of the Reynolds stress tensor using a summation of the orthonormal modes with the related time-dependent amplitude coefficients, whereas DMD modes are not orthonormal, and would not allow such a procedure. We thus focus on the mean kinetic energy (M.K.E.) transport equation:

$$0 = -\overline{u}_j \frac{\partial}{\partial x_j}\left(\frac{1}{2}\overline{u}_i\overline{u}_i\right) - \frac{\partial}{\partial x_i}\left(\overline{u}_i p\right) + \overline{u}_i \overline{F}_i + \frac{1}{Re}\nabla^2\left(\frac{1}{2}\overline{u}_i\overline{u}_i\right) - \frac{1}{Re}\frac{\partial \overline{u}_i}{\partial x_j}\frac{\partial \overline{u}_i}{\partial x_j} + \underbrace{-\frac{\partial}{\partial x_j}(\overline{u}_i\overline{u_i'u_j'}) - \frac{\partial}{\partial x_j}(\overline{u}_i\overline{\tau_{ij}^r}) + \overline{u_i'u_j'}\frac{\partial \overline{u}_i}{\partial x_j} + \overline{\tau_{ij}^r}\frac{\partial \overline{u}_i}{\partial x_j}}_{Turbulent\ M.K.E.\ flux} \tag{22}$$

where $\overline{\circ}$ indicates the time average, whereas prime denotes the fluctuations. Within the wake, as opposed to subgrid-scale stresses, which are negligible, turbulent M.K.E. flux is the most important term for wake recovery according to [20,38,45]. The following equation can be used to evaluate the total M.K.E. flux per unit area due to the turbulent fluctuations entering a generic closed surface S:

$$\mathfrak{F}_T = \frac{1}{S}\int_V -\frac{\partial}{\partial x_j}\left(\overline{u}_i\overline{u_i'u_j'}\right) dV, \tag{23}$$

where V is the volume enclosed by the surface S. Given the orthogonality of the POD modes, the Reynolds stress tensor can be rewritten as:

$$\overline{u_i'u_j'} = \overline{\sum_{k=1}^{N}\left(a_k\phi_i^k\right)\sum_{l=1}^{N}\left(a_l\phi_j^l\right)} = \sum_{k=1}^{N}\sum_{l=1}^{N}\overline{a_k a_l}\phi_i^k\phi_j^l = \sum_{k=1}^{N}\lambda_k\phi_i^k\phi_j^k, \tag{24}$$

to calculate the effect of each POD mode on the turbulent M.K.E. flux as follows:

$$\mathfrak{F}_T^k = \frac{1}{S}\int_V -\frac{\partial}{\partial x_j}\left(\overline{u}_i\lambda_k\phi_i^k\phi_j^k\right) dV. \tag{25}$$

This equation can be rewritten as a surface integral as:

$$\mathfrak{F}_T^k = \frac{1}{S}\int_S -\overline{u}_i\lambda_k\phi_i^k\phi_j^k\, dS_j. \tag{26}$$

A cylindrical domain of radius R_c and length L_c, centered in the rotor axis, is used to evaluate the turbulent M.K.E. flux through its lateral surface. The infinitesimal surface element dS is normal to the streamwise direction and is represented by the following vector:

$$dS = (0, dc_2, dc_3)\, dx, \tag{27}$$

where dc_2 and dc_3 are the vertical and transverse components, respectively, of the vector dc normal to the infinitesimal arc of the cylinder circumference C. The total turbulent M.K.E. flux per unit area over the

lateral surface of the cylinder can be calculated for each POD mode, as follows:

$$\mathfrak{F}_T^k = \int_{L_c} f_T^k(x)\, dx, \tag{28}$$

$$f_T^k(x) = -\frac{1}{2\pi R_c L_c} \int_C \overline{u}_i(x)\lambda_k \phi_i^k(x)\phi_j^k(x)\, dc_j. \tag{29}$$

The local fluxes $f_T^k(x)$ are calculated for a circumference of radius $R_c = 0.5$, whereas the total flux $\mathfrak{F}_T^k$ is calculated for different radii in the range $R_c \in [0.35\ 0.62]$. To circumvent a direct computation of the integrals over the cylindrical surfaces, the surface integral of the aforementioned Eq. (29) is transformed into a volume integral. This volume integral is subsequently evaluated numerically, using the midpoint rule on subintervals of length that are compatible with the grid size.

3. Simulation setup

3.1. Precursor simulations

This study aims at comparing the coherent structures in the wake of an NREL-5MW [29], generated in two different turbulent inlet conditions taking into account or not the Coriolis effect. For this purpose, two precursor simulations have been carried out. The first considers a neutral ABL flow driven by a pressure gradient in the absence of the Coriolis force ($f_c = 0$, $F_{PI} = 0$), which will be denoted in the following as the "pressure gradient" case. This case precludes consideration of the effects of the Earth's rotation and is therefore a simplification of the ABL. In practical terms, the equation for the conservation of momentum incorporates a term that refers to the pressure gradient. This term is calculated in such a way that the flow rate through the domain is kept constant.

The second precursor simulation, considering the effect of the Coriolis force, is driven by a geostrophic wind at the top of the domain, and will be characterized by a variation of the streamwise and spanwise components of the velocity in the wall-normal direction, as would occur in the Ekman spiral [46]. A Coriolis frequency $f_c \approx 1.2 \times 10^{-4}[s^{-1}]$ is assumed, which is a value typical of North Sea regions. Setting the geostrophic velocity components so that a certain desired flow direction can be defined is difficult due to the wind's dependence on altitude. For this reason, to avoid a yaw misalignment between the mean velocity profile at hub height and the wind direction, the PI controller proposed in Ref. [47] is adopted, which has been presented in Section 2.1. After the tuning of the PI controller, a proportional gain $K_P = 1$ and an integral gain $K_I = 0.1$ are chosen. The controller is stopped when $e(t) = \theta - \theta_{desired} < 0.1°$.

The computational domain of both the precursor simulations has dimensions $6 \times 11 \times 3$ diameter units in the streamwise (x), vertical (y), and spanwise (z) directions, respectively. Notice that to allow the Ekman layer to be fully developed up to the top boundary, the domain is chosen to be very large in the vertical direction compared to the previous LES of the same turbine [22]. A Cartesian grid with $1024 \times 512 \times 512$ points is chosen to discretize the box. Periodicity is applied in both the streamwise and spanwise directions, whereas no-slip and free-slip conditions are applied at the bottom and upper wall of the domain, respectively. The main features of the turbine are reported in Table 1; the corresponding Reynolds number is approximate of order 10^8.

3.2. Turbine flow simulations

The two ABL velocity profiles obtained by the precursor simulations are employed as inflow boundary conditions for the simulation of the flow impinging on the 5MW wind turbine. The computational box has dimensions $12 \times 11 \times 3$ diameter units. It is discretized using a staggered $2048 \times 512 \times 512$ points grid, with uniform spacing in the streamwise and spanwise directions, and stretching in the wall-normal direction, with a constant refined spacing in the rotor region. This grid has already been used in Ref. [10] and the results of the code validation study [37] indicate that the cell size employed in this study yielded satisfactory outcomes when compared to the experimental results. These simulations share the same boundary conditions as the precursor ones, except for the streamwise direction. The inlet condition for the two cases is the time-varying turbulent velocity obtained from the precursor simulations. A uniform convection velocity $c = 0.9\ U_{ref}$ is used as for the radiative outlet condition [48]. The immersed boundary method is used to represent the tower and nacelle, while the actuator line model is employed to simulate the turbine blades [40]. The rotor is positioned 4 diameters away from the inflow boundary and is centered in the spanwise direction. To allow the development of the wake, it is considered sufficient to have the outlet boundary at a distance of 8 diameters from the wind turbine. The wind turbine operates at its rated conditions.

Table 1
Main features of NREL 5-MW wind turbine.

	NREL 5-MW
Blades number	3
Rotor diameter - D [m]	126
Hub height [m]	90
Design Tip-Speed Ratio - TSR [–]	7
Rated wind speed - U_{ref} [m/s]	11.4
Rated rotor speed Ω [RPM]	12.1

4. Results

4.1. Precursor simulations

4.1.1. Time-averaged velocity fields

Mean velocity profiles are obtained from the precursor simulations by performing time (t) and spatial averaging along the horizontal ($x - z$) directions when statistically stationary conditions are reached. The averaged velocity (which is a function of the vertical direction only) is denoted as $\overline{u}, \overline{v}, \overline{w}$, where u, v, w are the instantaneous velocity components in the streamwise, vertical, and spanwise directions, respectively. Fig. 1 shows the mean velocity profiles of the axial and veer velocities and the wind direction $\overline{\theta} = \tan^{-1}(\overline{w}/\overline{u})$, expressed in degrees. The validation of the geostrophic forcing was previously established by comparing it with the results obtained from Ref. [49] (see Appendix A). The blue lines refer to the Coriolis case, whereas the orange ones are relative to the pressure gradient case. The black dash-dotted line is the log-law wind profile. Note that, due to the action of the PI controller of the wind direction, there is no yaw misalignment at the hub height. In the pressure gradient case, it can be seen that there is virtually no lateral wind component (see the orange lines in Fig. 1). The inner region of the two cases' curves in the left panel is well represented by the log-law profile. Fig. 2 illustrates in a 3D view the mean velocity profile obtained by the precursor simulation with geostrophic force. The black dashed line is the Ekman spiral, the red dash-dotted line, and the green dash-dotted lines refer to the spanwise and streamwise velocity components, respectively, and the black solid line is the ABL profile. A turbulence intensity of 7% is obtained at the hub height for both precursors.

4.1.2. POD and DMD modes

The POD and DMD analysis has been performed on the two datasets of the precursor simulations, one for Coriolis' case and one for the pressure gradient case. The snapshots of the velocity field have been extracted every $\Delta t = 0.025$ in a reduced domain of dimensions $[0 - 6] \times [0 - 1.55] \times [0.8 - 2.2]$ in the x, y, z directions, respectively. The datasets are both composed of 2370 snapshots each, from which the

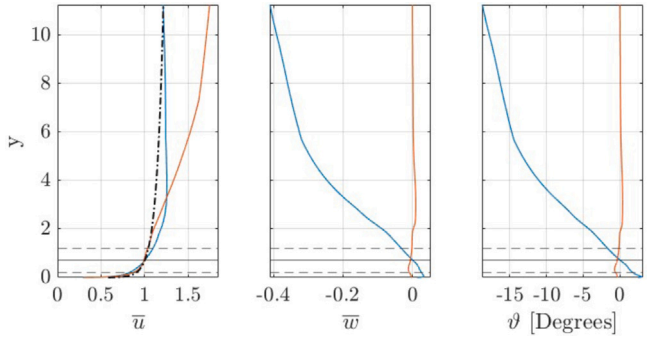

Fig. 1. Streamwise (left) and spanwise (center) components of the time- and horizontally-averaged velocity, and wind direction θ (right). The orange lines refer to the pressure gradient case, whereas the blue lines are relative to the Coriolis case. The black dash-dotted line is the log-law wind profile. The horizontal solid line indicates the hub height, whereas the dashed lines indicate the blade's tip. (For interpretation of the references to color in this figure legend, the reader is referred to the web version of this article.)

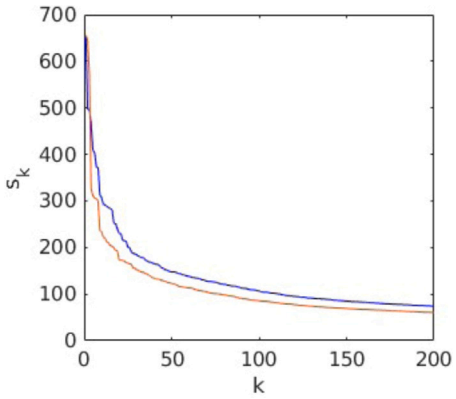

Fig. 3. Singular values of the first 400 POD modes for the pressure gradient (orange) and the Coriolis (blue) precursor cases. (For interpretation of the references to color in this figure legend, the reader is referred to the web version of this article.)

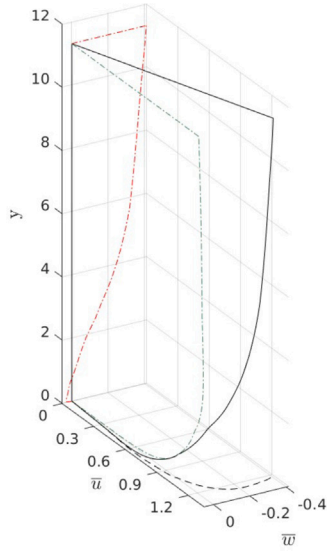

Fig. 2. Time- and horizontally-averaged dimensionless Coriolis ABL velocity profiles (black solid line). The green dash-dotted line is the $\overline{u}$-component, the red dash-dotted line is the $\overline{w}$-component and the black dashed line is the Ekman spiral. (For interpretation of the references to color in this figure legend, the reader is referred to the web version of this article.)

time-averaged velocity field has been subtracted. Fig. 3 illustrates the singular value distribution of the leading POD 400 modes. A notable reduction in energy is observed within the leading 20 modes, followed by a more gradual decrease.

Following the convergence analysis provided in the Ref. [10], a POD subspace of rank $r = 400$ is chosen for carrying out the DMD analysis. The complex frequency of the DMD modes, ω, is obtained using the eigenvalues μ of the linear operator $\tilde{A}$, computed as in Eq. (15). Therefore ω is computed as follows:

$$\omega = -\frac{log(\mu)}{i\Delta t}, \tag{30}$$

where Δt is the time interval between two successive snapshots and i is the imaginary unit. Notice that $\omega = \Re(\omega) + i\Im(\omega)$ is a complex number, so its real part is the angular frequency of the DMD mode, whereas the imaginary part is the growth rate. Fig. 4(a) shows the distribution of the angular frequency of the DMD modes for the two cases, along with the associated amplitudes for the DMD case without the sparsity promoting penalization (green dots) and with the SP algorithm (black lines) for a given value of the sparsity parameter. Without the sparsity penalization, we can observe that the distribution of the frequency for the two considered cases is rather similar, although one can observe that in the geostrophic forcing case, the peak amplitudes are recovered for larger values of $\Re(\omega)$ and for a broader range of frequencies.

The SP-DMD analysis has been carried out for the two considered precursor cases, and for different values of the sparsity coefficient. Since the dataset is significantly dissimilar, the algorithm selects a different number of modes between the two cases considered. This difference is most striking when a few modes are selected, namely for a large value of the sparsity parameter, *i.e.*, $\gamma = 10000$. For the pressure gradient-inflow case, only 6 DMD complex conjugate pairs of modes are selected, whereas in the Coriolis case, 12 mode pairs are selected (for visualization issues, in Fig. 4(a) and in the following ones we show only the modes with positive real parts). Considering the frequencies of the selected DMD modes, one can see in Fig. 4(a) that in the pressure gradient case, the highest frequency mode does not exceed $\Re(\omega) = 1.4$, whereas in the presence of the Coriolis force (Fig. 4(b)) this value is exceeded, indicating that a larger range of frequencies is needed for describing the dynamics. In both cases, the selected modes are characterized by rather low frequencies, as also observed in Ref. [10] in the presence of inflow turbulence.

Concerning the spatial structure of the selected DMD modes, Figs. 5 and 6 shows the isosurfaces of the streamwise velocity component for the 3 leading modes in the pressure gradient case, and for 4 of them in the Coriolis case. The orange surfaces refer to negative velocity fluctuations, whereas the blue surfaces refer to positive ones (note that the magnitudes of the velocities of each DMD mode have no physical meaning per se, as they should be multiplied by the amplitudes to reconstruct the data sequence). For both precursors, the lowest-frequency modes with $\Re(\omega) < 0.1$ are characterized by high- and low-speed large-scale streamwise-elongated streaks of spanwise size ≈ 1 (see Figs. 5(b) and 6(b)), which are known to form one of the two main elements of self-sustaining vortices that characterize the large scale motion in turbulent shear flows [50]. For the pressure gradient precursor, streamwise structures with large wavelength ($\lambda_x \approx 5$) characterize the DMD modes with frequency $\Re(\omega) \in [0.40 - 0.67]$ (see Fig. 5(a), as an example). The last two selected modes with $\Re(\omega) > 1.20$ (see Fig. 5(c)) have structures with slightly smaller wavelengths ($\lambda_x \approx 3$) and are constituted by positive/negative fluctuations alternating in the streamwise and spanwise directions. Notice also that all the selected modes cover the entire sub-domain, similar to the observations of De Cillis et al. [10] for a precursor simulation in the absence of wind veer.

When the geostrophic force is taken into account, the modes with frequency $\Re(\omega) \in [0.67 - 1.00]$ (see Fig. 6(a)) are associated with

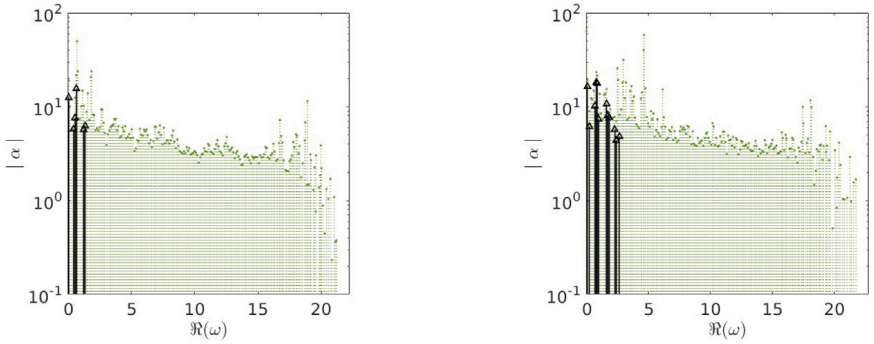

Fig. 4. Absolute value of DMD amplitudes α_i versus the angular frequency $\Re(\omega)$ for pressure gradient (a) and Coriolis (b) precursor cases. Green circles represent the DMD modes, whereas black triangles ($\gamma = 10000$) are the SP-DMD modes.

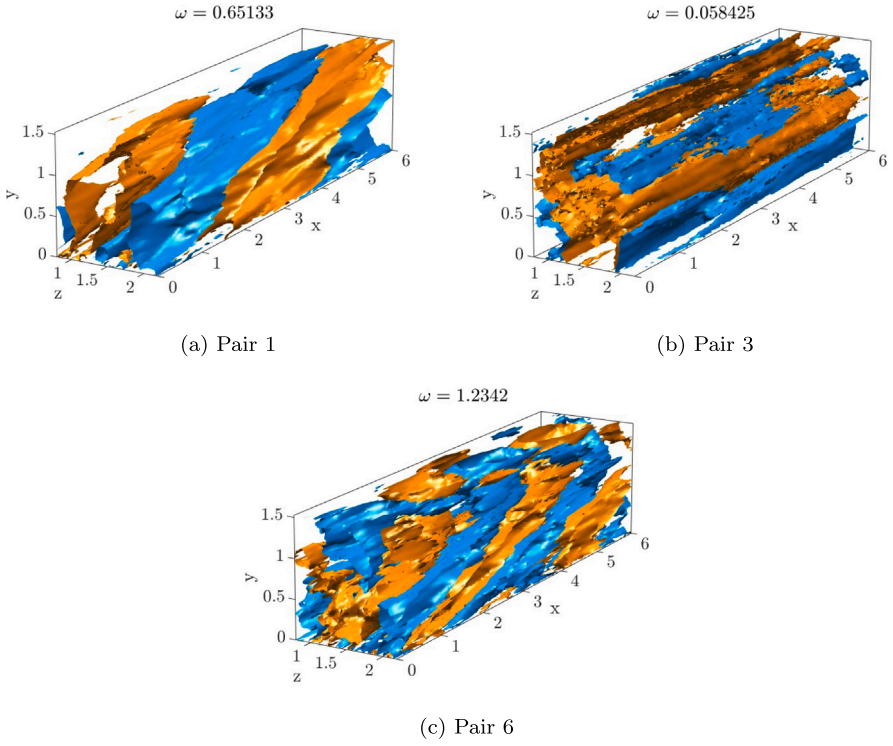

Fig. 5. Streamwise velocity fluctuation iso-surfaces for three modes selected by SP-DMD with $\gamma = 10000$ for the pressure gradient precursor simulation. The iso-surfaces colored in blue indicate a positive fluctuation $u = 0.0008$, whereas, the orange ones represent a negative fluctuation $u = -0.0008$. (For interpretation of the references to color in this figure legend, the reader is referred to the web version of this article.)

coherent structures alternated in the streamwise and spanwise directions with wavelengths of the order of ≈ 5. In contrast to the case without wind veer, the structures are not oblique. For frequencies $\Re(\omega) \in [1.62 - 1.85]$ (see Fig. 6(c)), streamwise-modulated velocity fluctuations are observed that are extremely similar to the previous case. In comparison to the previous case, frequency modes $\Re(\omega) > 2.0$ are also selected (see Fig. 6(d)). This corresponds to structures with wavelengths $\lambda_x \approx 2$ that cover the entire domain. It is evident that for both precursors the length scales of these flow structures ($\lambda_x \approx 5$ and $\lambda_z \approx 1-2$) exhibit a consistent correlation with the observed large-scale motions in turbulent channels and boundary layers [50,51].

4.2. Wind turbine's wake

4.2.1. Time-averaged velocity fields of turbine wakes

The spatial development of the wake structure of a wind turbine can be evaluated using an analysis of the time-averaged velocity field. When the incoming wind has no veer, the wake is nearly symmetric to the vertical axis. However, under geostrophic forcing, due to the effect of a significant cross-flow component [52], the rotor wake is highly skewed when advected downstream. Moreover, as already known, the presence of the tower leads to a strong deformation within the wake, especially in the case of geostrophic forcing. Figs. 7(a) and 7(b) show the Q-criterion iso-surfaces, colored by the values of the streamwise velocity in the pressure gradient-inflow case and the Coriolis case, respectively. It can be seen that in the absence of wind veer (Fig. 7(a)) proceeding along the domain, the wake remains aligned in the streamwise direction and is almost symmetrical to the vertical axis. Whereas, in the presence of geostrophic forcing, the wake is extremely deformed, assuming an almost elliptical shape downstream. Furthermore, again due to the cross-flow component, the tower wake undergoes a deflection in the positive lateral direction as it proceeds outwards.

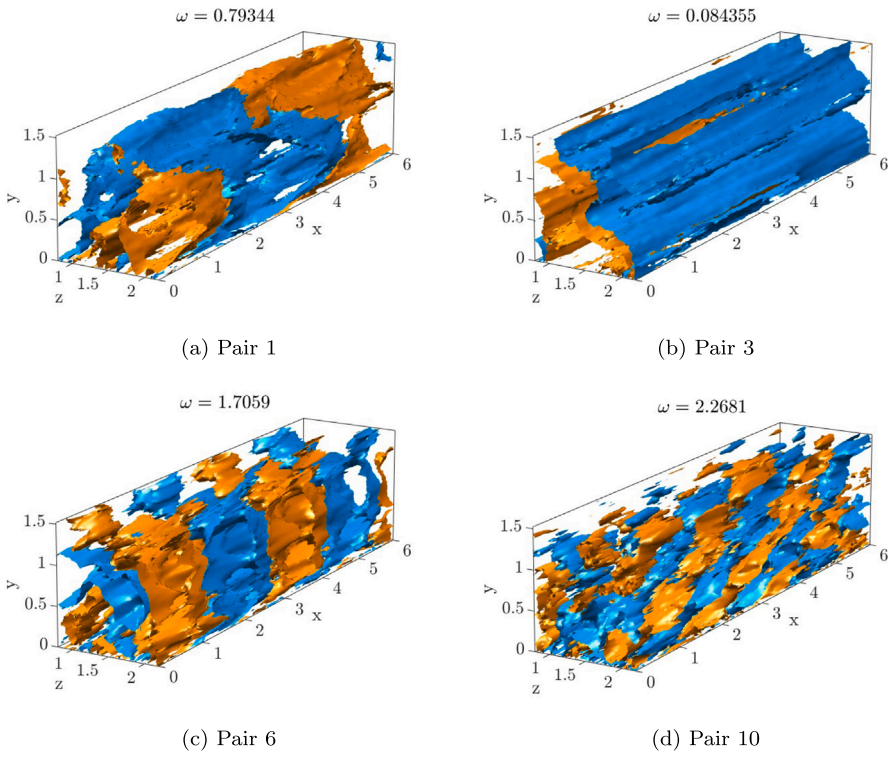

(a) Pair 1 (b) Pair 3

(c) Pair 6 (d) Pair 10

Fig. 6. Streamwise velocity fluctuation iso-surfaces for four modes selected by SP-DMD with $\gamma = 10000$ for the Coriolis precursor simulation. The iso-surfaces colored in blue indicate a positive fluctuation $u = 0.0008$, whereas, the orange ones represent a negative fluctuation $u = -0.0008$. (For interpretation of the references to color in this figure legend, the reader is referred to the web version of this article.)

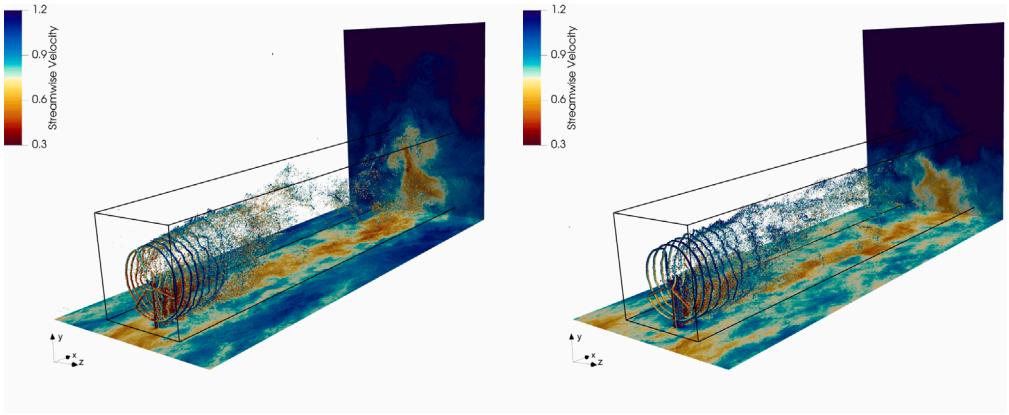

(a) (b)

Fig. 7. Q-criterion iso-surfaces, colored by the streamwise velocity values, for the pressure-gradient (a) and Coriolis case (b). The box sketches the dimensions of the subdomain in which the modal decompositions are performed.

The same conclusions can also be reached by observing the velocity loss within the wake, defined as $\Delta u = u_{in} - u$, where u_{in} is the time-averaged streamwise inflow velocity, in the absence (Fig. 8(a)) and in the presence (Fig. 8(b)) of wind veer. While in the former case, the wake maintains its circular shape as one proceeds downstream, in the case with the wind veer, moving away from the rotor, the wake tends towards an elliptical shape. The results, compared to those of Abkar [13], show an excellent similarity, although, given the presence of the tower, the deformation is greater as the wake advances.

4.2.2. POD and DMD modes

Two datasets, both containing 2370 snapshots, one for the Coriolis inflow case and the second for the pressure gradient one, have been used for the POD and SP-DMD analyses of the wind turbine's wake. Snapshots of the velocity field have been extracted at regular intervals $\Delta t = 0.0125$, corresponding to 10° rotation of the blades in a reduced domain of dimensions $[3.8-11.9]\times[0-1.55]\times[0.8-2.2]$ in the x, y, and z directions, shown by the box in Fig. 7. The time-averaged velocity field has been subtracted from each snapshot.

Fig. 9 shows the singular value distribution for the first 600 POD modes. There is a sharp decrease in energy in the first $\approx$ 10 modes, followed by a slower decrease. Following the convergence analysis provided in the Ref. [10] since a plateau is reached in correspondence of the $\approx$ 600th mode, a basis with $r = 600$ POD modes has been considered for performing the DMD analysis.

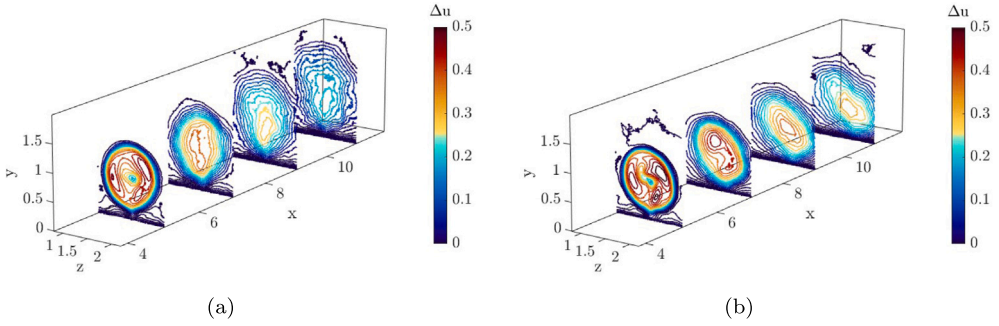

Fig. 8. Time-averaged streamwise velocity-loss field obtained by LES, in the $y-z$ plane at $x = 5, 7, 9, 11$ diameter units downstream of the wind turbine for (a) the pressure gradient-inflow case and (b) the Coriolis-inflow case.

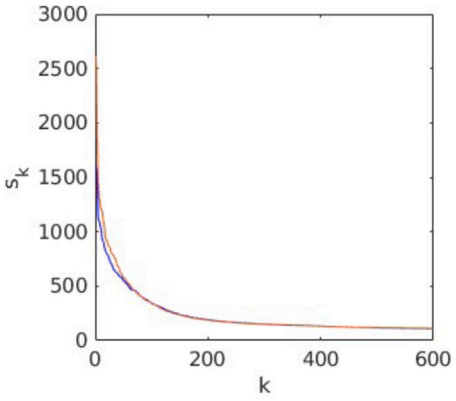

Fig. 9. Singular values of the first 600 POD modes for the pressure gradient (orange) and the Coriolis (blue) wind turbine cases. (For interpretation of the references to color in this figure legend, the reader is referred to the web version of this article.)

Figs. 10(a) and 10(b) show the absolute values of DMD amplitudes α_i versus the angular frequency $\Re(\omega)$ for the pressure gradient case and the Coriolis case, respectively. For both figures, green circles are associated with the DMD modes, whereas the results of the sparsity-promoting algorithm are given by the red circles for $\gamma = 33500$, black circles for $\gamma = 21300$ and blue triangles for $\gamma = 10000$. An increase of the sparsity coefficient γ corresponds to sparser solutions. This means that a smaller subset of modes is selected by the algorithm, corresponding to the more dynamically relevant coherent structures, along with their optimized values of α. Notice that in both cases, the algorithm selects only low-frequency modes for the larger value of γ, whereas it picks one or two high-frequency modes for lower values of the sparsity parameter. In the pressure gradient case, only for the lowest values of $\gamma = 10000$ a high-frequency mode is selected by SP-DMD. In particular, the algorithm selects the mode associated with $\Re(\omega) = 42$, which is related to tip vortices and corresponds to three times the angular frequency of the turbine. It is thus observed that for the same sparsity coefficient, coherent structures related to higher frequencies are more relevant to the turbine dynamics when the Coriolis force is considered. In contrast, for the case without wind veer, low-frequency structures are more representative. From now on, the discussion of the results will be based on the case with sparsity coefficient $\gamma = 33500$. It should be noted that, for the same value of γ, the sparsity-promoting algorithm selects 5 mode pairs for the pressure gradient case and 7 for the Coriolis case. This indicates that, in the latter case, there is a greater number of non-negligible modes, especially in the high-frequency range, because the dynamics of the flow is more complex. A similar disparity in mode numbers has been observed in the precursor simulation results. This might have been expected looking at the frequency distribution of the DMD modes in the absence of penalization of the number of modes (green circles in Fig. 10(b) for the Coriolis case), showing high amplitudes for a much larger range of frequencies with respect to the pressure gradient case shown in Fig. 10(a). Table 2 gives a small summary of the frequencies of the first 10 modes as the sparsity coefficient varies for the two cases analyzed.

The spatial structure of the selected modes will be now discussed. In the case of the pressure gradient, all the modes selected by the SP-DMD algorithm have low frequencies in the range $\Re(\omega) \in [0.45 - 5.57]$, which are associated with coherent structures of different scales covering the entire domain. Modes with frequency $\Re(\omega) \in [0.45 - 0.67]$ are associated to structures with large length scale $\lambda_x \approx 7.5$ (see Fig. 11(a)). Whereas for $\Re(\omega) = 1.45$ and in the range $\Re(\omega) \in [3.20 - 5.50]$ moderate length scale structures ($\lambda_x \approx 3.7$ and $\lambda_x \approx 1.6$, respectively) are seen in Figs. 11(c) and 11(d). Fig. 11(b) shows that for frequencies $\Re(\omega) \approx 5.50$, structures characterized by wavelengths smaller than ≈ 1 are observed. In general, the presence of the turbine does not result in the formation of a discernible geometric pattern linked to the presence of the blades and/or tower/nacelle in the selected modes. Concerning the Strouhal numbers St of these modes, it is of interest to ascertain whether they correspond to the wake meandering values obtained in recent studies [53,54]. For modes with $\Re(\omega) < 1$, as also demonstrated by De Cillis et al. [10] in their study about the same reference turbine, but in the absence of the Coriolis force, a Strouhal number of $St \leq 0.2$ is found. This is in line with the typical frequency ranges of wakes observed in the literature. This confirms the conjecture made in several literature studies, that wake meandering is more likely to be the consequence of an external factor, associated with the turbulent nature of the ABL, rather than an effect linked to the turbine itself.

Considering now the case with Coriolis inflow for frequencies $\Re(\omega) < 1$, the resulting structures exhibit a streamwise length mostly equal to that of the sub-domain $\lambda_x \approx 7.4$, as shown in Fig. 12(b). Coherent structures of medium wavelengths ($\lambda_x \approx 3.4$) are observed for the modes in the range $\Re(\omega) \in [1.50 - 1.90]$, whereas structures with a length scale of order $1.5 - 2$ are correlated with $\Re(\omega) \in [2.87 - 4.62]$ (see Figs. 12(a) and 12(c), respectively). Fig. 12(d) shows the DMD mode with $\Re(\omega) \approx 42$, which corresponds to an angular frequency of three times the rated value of the turbine. Notice that, with a lower sparsity coefficient the algorithm would select the mode with a frequency of ≈ 84, which is six times the turbine rotation frequency. This high-frequency mode is associated with the tip vortices. Regarding the Strouhal number, the value reported for the pressure gradient case is recovered also when the Coriolis effect is present. It can be observed that in the pressure gradient case, the high-frequency modes related to tip vortices are more easily discarded by the SP algorithm as the sparsity parameter is increased. In contrast, the addition of a wind veer preserves such high-frequency wave structures to a greater extent. It may thus seem that the presence of wind veer delays the breakdown of such structures, maybe providing a negative effect on wake recovery, as it will be investigated in Section 4.2.4. It is noteworthy that, as

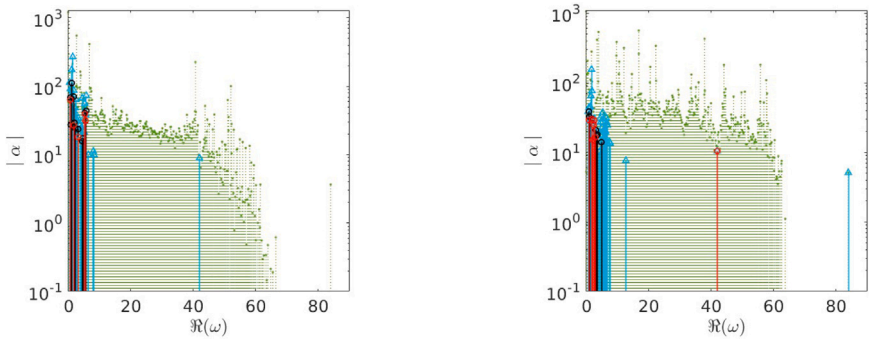

Fig. 10. Absolute value of DMD amplitudes α_i versus the angular frequency $\Re(\omega)$ for the pressure gradient (a) and the Coriolis (b) turbine's wake cases. Green circles represent the DMD modes, whereas blue triangle ($\gamma = 10000$), black circles ($\gamma = 21300$), and red circles ($\gamma = 33500$) are the SP-DMD modes. (For interpretation of the references to color in this figure legend, the reader is referred to the web version of this article.)

Table 2
Frequencies of the first 10 modes selected by the SP-DMD algorithm for different sparsity coefficients, for both wind turbine's flow cases considered.

	Pressure gradient			Coriolis		
	$\gamma = 10000$	$\gamma = 21300$	$\gamma = 33500$	$\gamma = 10000$	$\gamma = 21300$	$\gamma = 33500$
1st mode	2.6944	1.1271	0.6703	1.7443	0.9013	1.8870
2nd mode	1.4539	1.7749	5.3333	1.8870	1.0643	0.9013
3rd mode	1.1271	0.6703	5.5488	1.5741	1.8870	2.6218
4th mode	0.4676	5.7808	1.7749	1.3671	2.6218	2.4076
5th mode	0.6703	5.3332	3.2131	0.9013	2.4073	2.8588
6th mode	1.7749	5.5488	–	0.68845	3.0971	4.6195
7th mode	5.7808	2.0448	–	5.3586	3.6489	42.0000
8th mode	0.8426	0.8426	–	6.4352	3.3264	–
9th mode	4.4801	2.2016	–	4.4959	2.8588	–
10th mode	2.4539	3.2131	–	2.6218	2.1559	–

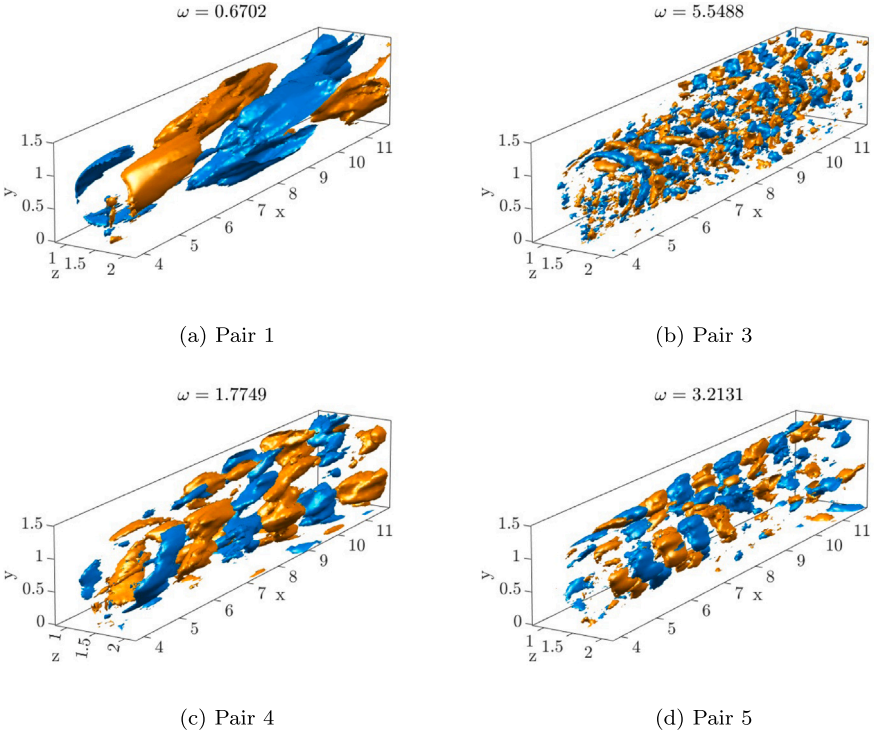

Fig. 11. Streamwise velocity fluctuation iso-surfaces for three modes selected by SP-DMD with $\gamma = 33500$ of pressure gradient-inflow turbine's wake simulation. The iso-surfaces colored in blue indicate a positive fluctuation $u = 0.001$, whereas, the orange ones represent a negative fluctuation $u = -0.001$. (For interpretation of the references to color in this figure legend, the reader is referred to the web version of this article.)

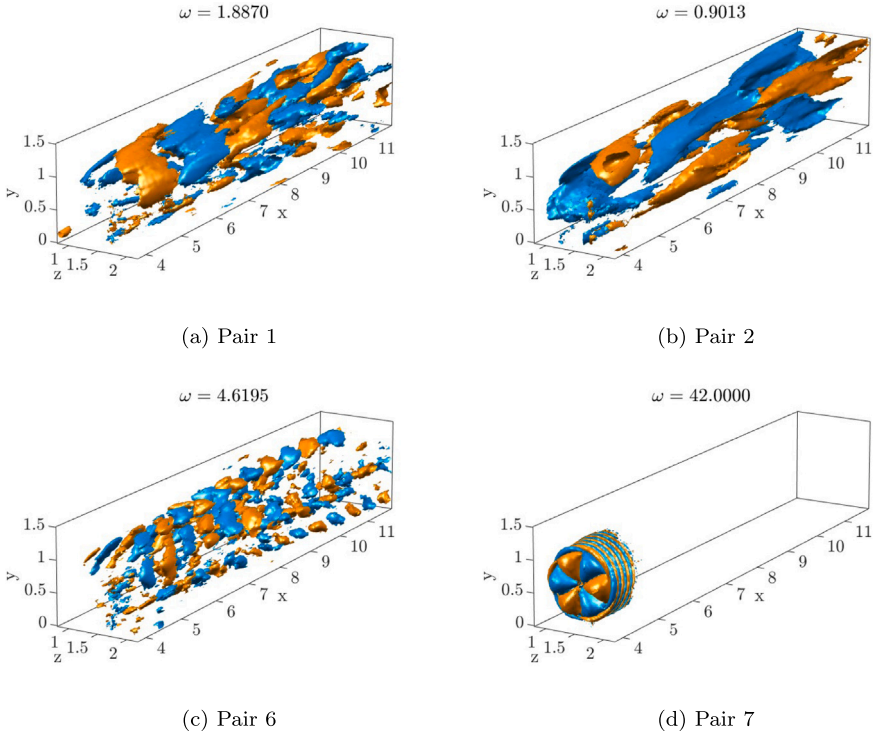

(a) Pair 1 (b) Pair 2

(c) Pair 6 (d) Pair 7

Fig. 12. Streamwise velocity fluctuation iso-surfaces for three modes selected by SP-DMD with $\gamma = 33500$ of Coriolis-inflow turbine's wake simulation. The iso-surfaces colored in blue indicate a positive fluctuation $u = 0.001$, whereas, the orange ones represent a negative fluctuation $u = -0.001$. (For interpretation of the references to color in this figure legend, the reader is referred to the web version of this article.)

one moves away from the rotor region, the structures extend towards the left region of the computational domain. Furthermore, the same structures in the far-wake region demonstrate that the wake of the tower is not centered in the z-direction (see Fig. 12(c)). Fig. 13 provides further evidence that streamwise fluctuation structures are strongly influenced by the presence of the wind veer. The figure displays three slices in $x - z$ planes at varying elevations for both inflow scenarios, using the 4th pair mode for the pressure gradient and the 1st pair mode for the Coriolis case, respectively. In Fig. 13(b) one can see that the Coriolis case exhibits a deflection of the structures towards the right below the hub height, whereas this trend is not apparent in the case without wind veer (see Fig. 13(a)). The same can be observed in the bottom figures (Figs. 13(e) and 13(f)), with the deflection occurring in the opposite direction. Whereas, at hub height (Figs. 13(c) and 13(d)), as expected due to the absence of wind veer, there is no deflection in either case.

The principal distinguishing feature between these two scenarios is the presence of a spanwise velocity component within the inflow. It would therefore be pertinent to undertake a study of the isosurfaces of the transverse velocity component within the wake. In the first case under consideration, it can be observed that coherent structures related to lateral velocity are rather weak at frequencies $\Re(\omega) < 1.45$ as shown in Fig. 14(a). Indeed, for high-frequency modes, it is possible to identify relevant flows, although these are mainly confined to the wake region away from the tower (see Fig. 14(b)). In the presence of the Coriolis force, on the contrary, transverse flow is prevalent. It can be observed in Fig. 15(a) that the structures exhibit an oblique shape, reminiscent of the deformation that is dictated by the Coriolis effect, as shown in Figs. 15(a) and 15(b). An intriguing observation is that, in contrast to the streamwise velocity component, the low-frequency spanwise structures exhibit minimal influence from the tower, nacelle, and rotor (see Fig. 15(a)). Whereas, for frequencies $\Re(\omega) > 3.10$, the presence of the tower and nacelle exerts a non-negligible influence on the flow, as evidenced by the iso-contours of the spanwise velocity component in Fig. 15(b).

It can be generally stated that the spanwise component of the velocity plays a significant role in the formation of coherent structures in the wake of a wind turbine, due to the effect of the Coriolis acceleration. This suggests that the veer exerts a pronounced effect on the wake. A comparison of the velocity components of the relevant DMD modes indicates that, in such a case, the streamwise and spanwise components are of comparable amplitude and extension. Consequently, in the case of a velocity profile exhibiting a notable cross-flow velocity component, it becomes evident that the exchange of momentum in the spanwise direction cannot be overlooked. Concerning the wavelengths associated with the DMD modes, it can be observed that both components exhibit values that are highly similar in both case studies. This similarity is more evident in the Coriolis case, as the structures related to the spanwise component are more developed, especially at low frequencies. This is another indication of how coherent structures in both directions have a significant effect on the evolution of the wake within the considered sub-domain.

4.2.3. Mean kinetic energy entrainment

Applying the procedure described in Section 2.4, based on the decomposition of the turbulent mean kinetic energy flux, we now analyze the contribution of the most energetic coherent structures to the wake recovery. As previously discussed, the main POD modes are used for this analysis, due to their orthogonality and to their energetic content. Fig. 16(a) shows the turbulent M.K.E. local flux results for the pressure gradient-inflow case. The local flux at $R_c = 0.5$ indicates that the 5 low frequency most energetic POD modes provide a positive M.K.E. local flux. For all these modes, the local flux has a peak in the near wake and decreases towards the far wake. Each mode peaks at a different streamwise location, between 7 and 10 diameters. Fig. 16(b) shows the total flux for different values of R_c. Again, the contribution of the five most energetic POD mode pairs is plotted. All modes contribute positively to the M.K.E. entrainment, in particular the first two. Turning instead to the results for the case with Coriolis-inflow, also in this case the first five pairs of modes provide a positive contribution to the

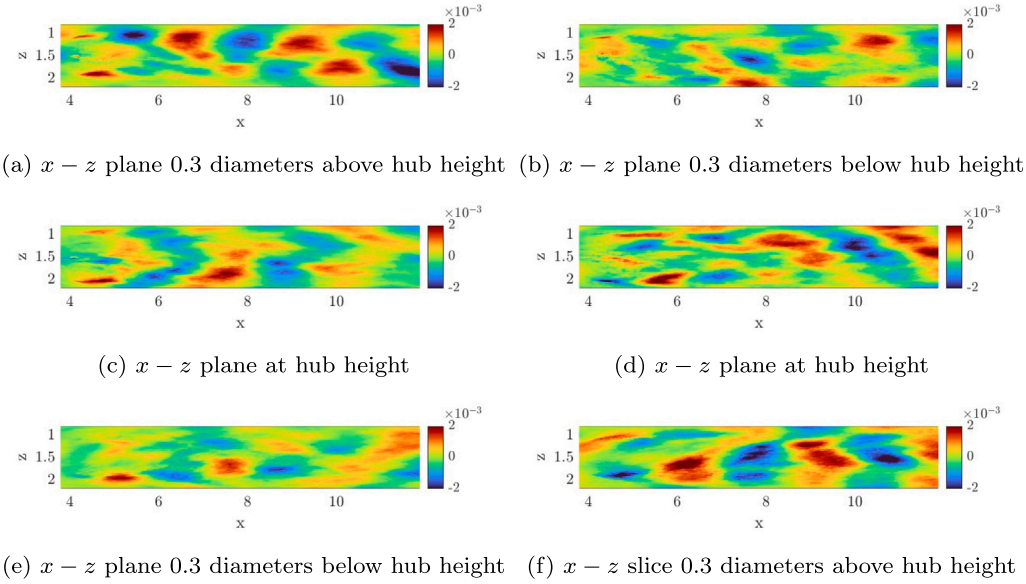

Fig. 13. Streamwise velocity fluctuation in $x-z$ planes at three different heights of the 4th mode pair of the pressure gradient case (left) and of the 1st mode pair of Coriolis turbine's wake case (right).

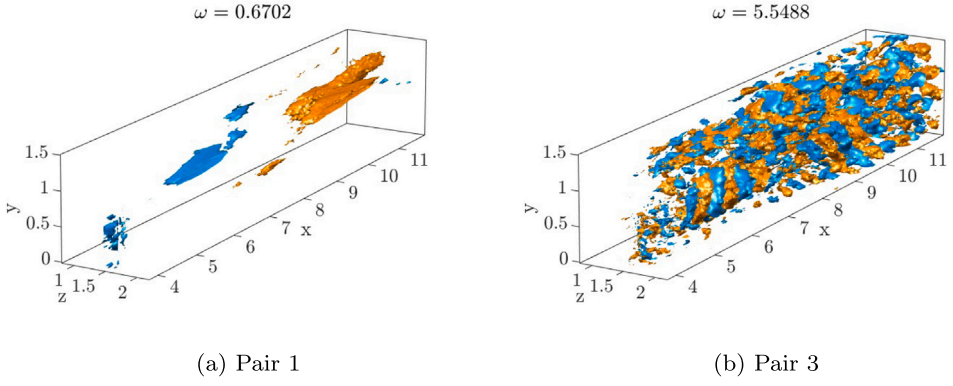

Fig. 14. Spanwise velocity fluctuation iso-surfaces for three modes selected by SP-DMD with $\gamma = 33500$ for the pressure gradient-inflow turbine's wake simulation. The iso-surfaces colored in blue indicate a positive fluctuation $w = 0.001$, whereas, the orange ones represent a negative fluctuation $w = -0.001$. (For interpretation of the references to color in this figure legend, the reader is referred to the web version of this article.)

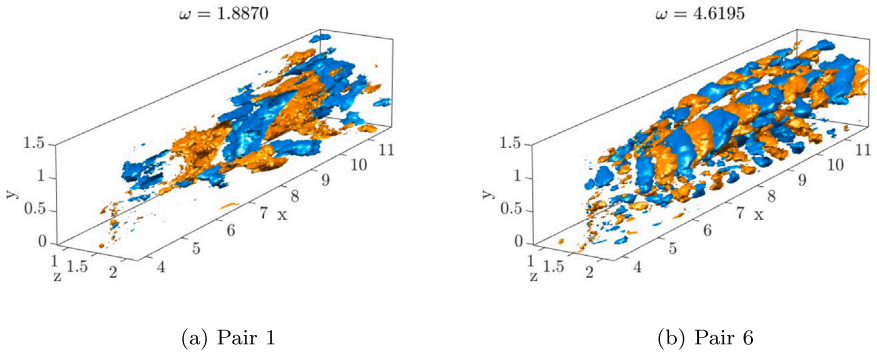

Fig. 15. Spanwise velocity fluctuation iso-surfaces for three modes selected by SP-DMD with $\gamma = 33500$ for the Coriolis-inflow simulation. The iso-surfaces colored in blue indicate a positive fluctuation $w = 0.001$, whereas, the orange ones represent a negative fluctuation $w = -0.001$. (For interpretation of the references to color in this figure legend, the reader is referred to the web version of this article.)

M.K.E. flux both locally and in total. Fig. 17(a) shows, compared with the previous case, a greater concentration of local flux peaks around $x \approx 6-7$. About the total flux (Fig. 17(b)), it can be observed that the M.K.E. entrainment peaks at $R \approx 0.5$ and decreases for $R > 0.5$ more rapidly than in the pressure gradient case. This means that the wind veer promotes the entrainment in the inside part of the wake, but this effect rapidly decays in the radial direction. As also shown in Fig. 7, the wake is more flattened compared to the pressure gradient case, so M.K.E. entrainment is more localized in space. Moreover, also in this case, the leading mode exerts a stronger influence on this quantity with

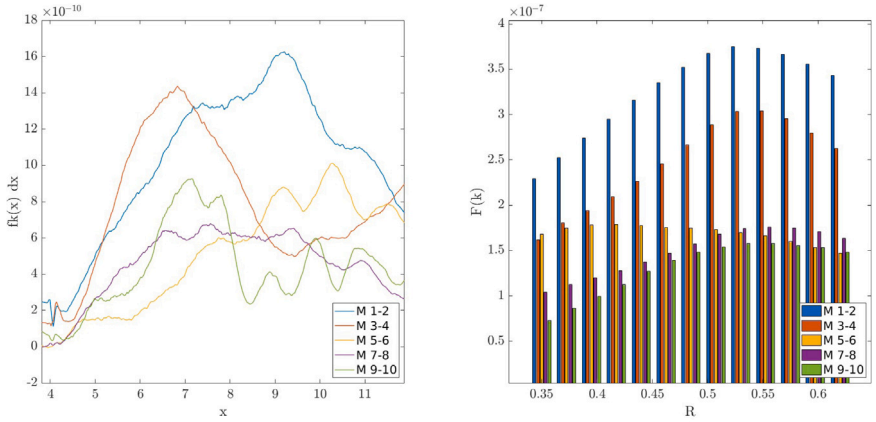

Fig. 16. M.K.E. entrainment for Pressure gradient-inflow case: (a) local (at $R_c = 0.5$) and (b) total fluxes.

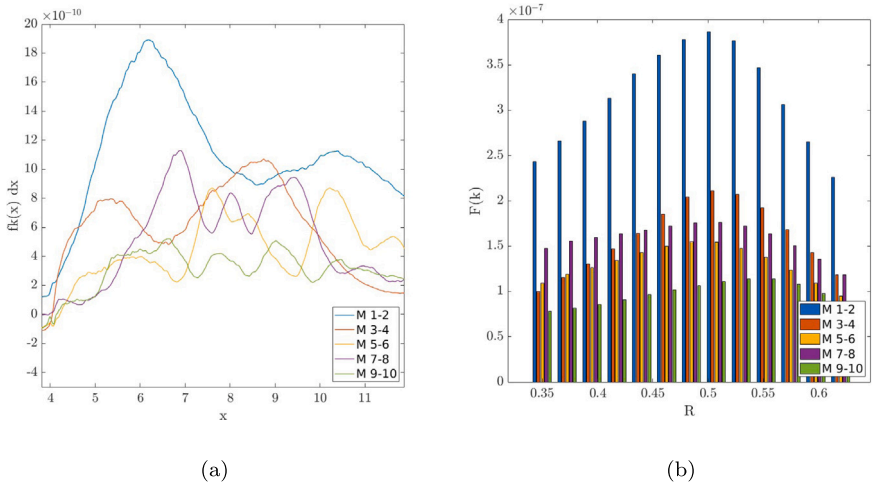

Fig. 17. M.K.E. entrainment for Coriolis-inflow case: (a) local (at $R_c = 0.5$) and (b) and total fluxes.

respect to the following modes. In the case of the pressure gradient, in comparison to the Coriolis one, the second mode exerts a more pronounced influence on the total flux. It is also of particular interest to note that the first two modes are similar for the two cases, but they are switched in terms of energy relevance, as one can see comparing Fig. 18 with Fig. 19, in which the first two mode pairs are shown for these two flow cases. One can observe that the mode with the longer wavelength is the most energetic for the pressure gradient case (Fig. 18(a)), whereas the mode with the medium wavelength is the more relevant one in the presence of the Coriolis effect (Fig. 19(a)).

4.2.4. Wakefield reconstruction

One of the most pertinent reasons for conducting a DMD analysis is the potential to derive reduced-order models allowing to reproduce accurately the evolution of a dynamic system at times larger than those used for the derivation of the model itself, thereby significantly reducing the overall computational cost. However, it is essential to recognize that an optimal value must be identified for the number of DMD modes selected and the resulting approximation error, which is calculated as follows:

$$error[\%] = \frac{1}{N}\sum_{j=1}^{N}\frac{\|q^j_{CFD} - x^j_{ROMF}\|}{\|q^j_{CFD}\|} \times 100, \tag{31}$$

where q^j_{CFD} is the jth snapshot obtained from the simulation and x^j_{ROMF} is the reconstructed flow field at the same time instant, obtained using Eq. (17).

Table 3 provides the error between the reconstruction and the actual dataset for the two flow cases under consideration, as a function of the number of modes selected by the SP algorithm. It can be observed that for an identical number of SP-DMD modes, the reconstruction for the scenario involving wind veer exhibits a slightly larger degree of accuracy in comparison to the pressure gradient case. Obviously, in both flow cases, the error increases as the number of selected modes decreases. However, the deviation of the reconstruction from the flow field remains rather small even for a very small set of DMD modes, namely for only 12 complex conjugate mode pairs. Depending on the required accuracy and the necessity of reducing the order of the model for computational purposes, one can choose an optimum number of modes for composing the desired reduced-order model. Fig. 20 shows the slices of the velocity field in the x–y plane of the snapshot of the original dataset (first row) and of the reconstruction with different numbers of SP-DMD modes (from the second to the fourth row, for a decreasing number of modes), for both flow cases considered. In all cases, the spatial structure of the reconstructed wakefield practically coincides with that of the LES snapshot when 600 dynamic modes (*i.e.*, 300 complex conjugate pairs) are retained. As the number of selected modes decreases, the small-scale vortex structure of the wake begins to be more poorly reconstructed. When only 12 mode pairs

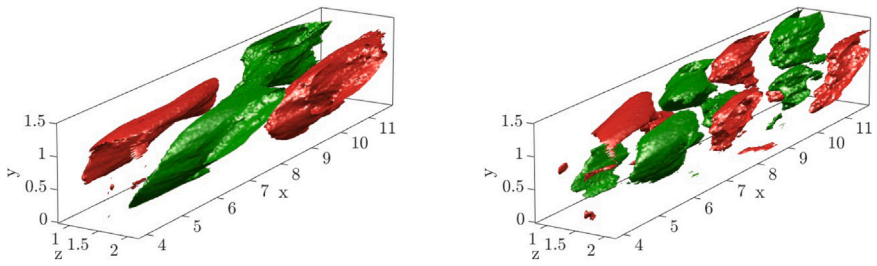

(a) Pair 1 (b) Pair 2

Fig. 18. Streamwise velocity fluctuation iso-surfaces for the first 2 POD modes of the pressure gradient-inflow turbine's wake simulation. The iso-surfaces colored in green indicate a positive fluctuation $u = 0.001$, whereas, the red ones represent a negative fluctuation $u = -0.001$. (For interpretation of the references to color in this figure legend, the reader is referred to the web version of this article.)

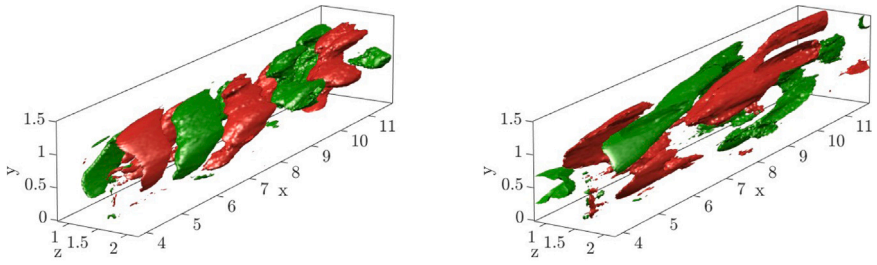

(a) Pair 1 (b) Pair 2

Fig. 19. Streamwise velocity fluctuation iso-surfaces for the first 2 POD modes of Coriolis-inflow turbine's wake simulation. The iso-surfaces colored in green indicate a positive fluctuation $u = 0.001$, whereas, the red ones represent a negative fluctuation $u = -0.001$. (For interpretation of the references to color in this figure legend, the reader is referred to the web version of this article.)

Table 3
Comparative analysis of the error of the DMD flow field reconstructions with respect to the original snapshot for the pressure gradient and Coriolis flow cases, as a function of the number of DMD mode pairs selected by the sparsity promoting algorithm.

	Pressure gradient	Coriolis
300 mode pairs	6.75%	4.79%
75 mode pairs	7.14%	5.25%
12 mode pairs	12.5%	8.87%

are retained, the small-scale flow structures appear to be completely smoothed out, despite the reconstructed flow structure maintaining remnants of the large-scale structures of the original snapshots. Overall, it is possible to conclude that a reconstruction based on 75 DMD mode pairs is appropriate to reproduce with a sufficient (5–7%) accuracy of the flow structure up to the small scales.

5. Conclusions

The main contribution of the present paper is the analysis of the impact of wind veer due to Coriolis acceleration in the atmospheric boundary layer (ABL) on coherent structures in the wake of the NREL 5 MW reference wind turbine. Large-Eddy Simulations (LES) of the flow through the wind turbine is carried out by solving the filtered Navier–Stokes equations for incompressible flows. Using the Dynamic Mode Decomposition (DMD) method, the most relevant mono-frequency modes are extracted from the wake, allowing us to decompose the turbulent wake in a set of coherent structures. Moreover, using a constrained minimization of the reconstruction error with a sparsity parameter (SP), a limited number of DMD modes are retained, reducing the number of relevant flow features that optimally approximates the original data sequence. The SP-DMD method is employed to compare the results with those obtained when wind veer is neglected, and to reconstruct the flow field, providing an efficient reduced-order model of the turbine's wake taking into account the wind veer.

In particular, a comparison of the velocity components of the DMD modes in the absence and in the presence of the Coriolis effect reveals that the presence of wind veer results in a greater relevance of the spanwise velocity component in the coherent structures and the increase of oblique flow features. The dynamically most significant DMD modes have a spanwise component of the velocity similar in amplitude and extent to the streamwise component. On the contrary, in the pressure gradient case, these transverse flow structures are not very significant and sometimes do not even form, especially for modes characterized by low frequencies. In the former case, these structures have an oblique trend in the far wake, following the distortion caused by the Coriolis effect.

For both flow cases, low-frequency flow structures, primarily determined by the turbulent inflow boundary layer's properties, dominate the wake. In contrast, coherent structures endogenously produced by the turbine, such as hub and tip vortices, are less important dynamically. However, the coherent structures of most modes recovered in the pressure gradient case show a stronger footprint of the presence of the tower.

For evaluating the effect of the coherent structures on the wake recovery, a Proper Orthogonal Decomposition (POD) is carried out in order to identify the effect of each POD mode on the mean kinetic energy entrainment. For this analysis, the POD method has been employed because it extracts the modes that contain the most energy and since it provides an orthonormal basis for the mean kinetic energy decomposition. The analysis of the main POD modes shows that the first two modes are similar in the two considered flow cases but are switched in terms of kinetic energy relevance. For the pressure gradient case, the higher-wavelength mode is the most important in terms of kinetic energy entrainment, but also the following modes (in terms of energy content) provide a rather large contribution to the wake

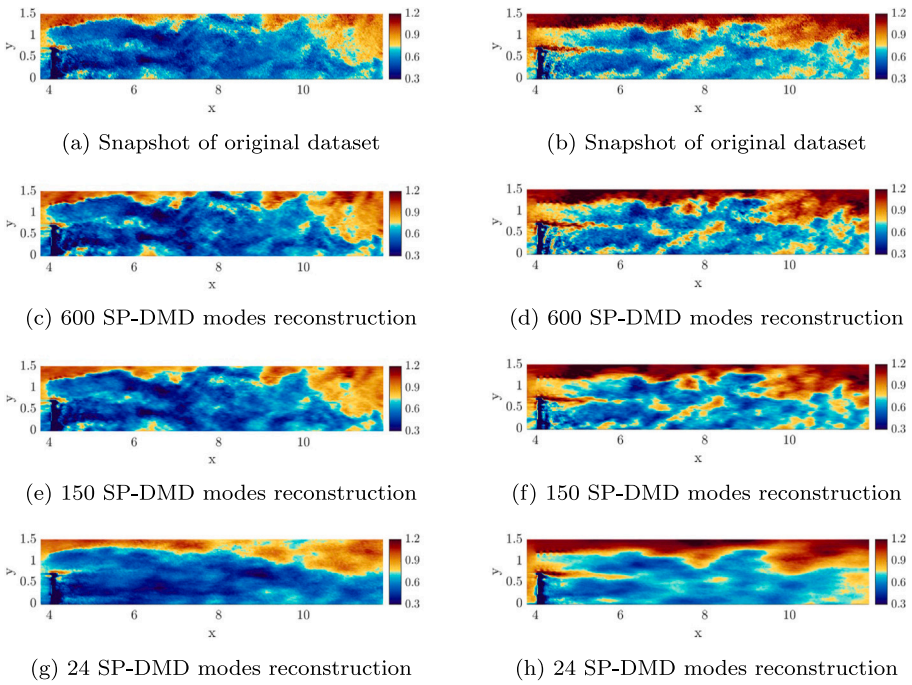

(a) Snapshot of original dataset (b) Snapshot of original dataset

(c) 600 SP-DMD modes reconstruction (d) 600 SP-DMD modes reconstruction

(e) 150 SP-DMD modes reconstruction (f) 150 SP-DMD modes reconstruction

(g) 24 SP-DMD modes reconstruction (h) 24 SP-DMD modes reconstruction

Fig. 20. Pressure gradient (left) and Coriolis (right) wakefield reconstruction results: original snapshot (a,b), wakefield reconstructed by SP-DMD with different number of modes (c–h).

recovery. Whereas, for the Coriolis case, the most important mode for wake recovery has a lower wavelength, and contributes to the wake recovery with an energy entrainment which is twice as large as that of the slightly less energetic modes. Moreover, in this last case, the peak of energy entrainment is localized mostly in the near wake, and at a lower radius than in the pressure gradient case, inducing a flatter wake downstream, as currently observed in the presence of wind veer.

As previously mentioned, another main contribution of the present work is the construction of an accurate reduced-order model of the wake of wind turbines based on the DMD modes. Such a model incorporates the characteristics of the turbulence entering the boundary layer and the potential influence of Coriolis acceleration. For a substantial number of modes selected by the SP-DMD algorithm, large-scale and small-scale vortex structures are both reconstructed with a high degree of accuracy, with an error on the L2-norm of the velocity field of only $\approx$ 5%. The latter structures are more susceptible to the choice of the number of modes. Indeed, as the number of modes decreases, the quality of reconstruction of these small-scale structures deteriorates. The discrepancy between the reconstruction and the original dataset increases as the number of modes in the reduced-order model decreases, reaching for only 12 mode pairs an error of $\approx$ 10%. Overall, it is possible to conclude that a reconstruction based on $\approx$ 70 DMD mode pairs is appropriate to reproduce with sufficient accuracy (corresponding to an error of 5–7%) the flow structure up to the small scales.

Through this in-depth study of the wake of a wind turbine under two different inflow conditions, namely in the presence and absence of a wind veer, it can be concluded that to achieve a realistic flow reconstruction, in light of the aforementioned considerations, it is advisable to incorporate the Coriolis force into a reduced-order model, given that the spanwise component of the velocity exerts a significant influence on the coherent structures generated by both the turbine blades and the ABL.

Although in the present study we have considered an NREL 5MW wind turbine, the effects of wind veer may be even stronger on larger-rotor turbines, for instance, the 15MW or 22MW NREL reference wind turbines, whose diameters are more than twice that of the considered turbine. Our results show that, also for the considered turbine, the wind veer due to the Coriolis force has a remarkable influence on the shape of the wake and on the dynamics of its coherent structures. Future work will be dedicated to the analysis of larger wind turbines, such as the NREL 15 MW wind turbine, and to interaction of multiple wind turbines in the presence of wind veer.

CRediT authorship contribution statement

Felice Manganelli: Writing – original draft, Validation, Software, Methodology, Investigation, Formal analysis. **Claudio Bernardi:** Software, Methodology. **Alessandro Giannotta:** Methodology, Formal analysis. **Stefano Leonardi:** Supervision, Software, Methodology, Conceptualization. **Stefania Cherubini:** Writing – review & editing, Supervision, Investigation, Conceptualization. **Pietro De Palma:** Writing – review & editing, Supervision, Investigation, Conceptualization.

Declaration of competing interest

The authors declare that they have no known competing financial interests or personal relationships that could have appeared to influence the work reported in this paper.

Acknowledgments

This study has been partially funded under the National Recovery and Resilience Plan (NRRP), Mission 4 Component 2 Investment 1.3 - Call for tender No. 1561 of 11.10.2022 Project code PE0000021, Project title “Network 4 Energy Sustainable Transition – NEST”, and under the PRIN grant 20229YJP33, “Diffuser augmented Wind Turbines for URBban environments” (DWTURB). Both are grants of Ministero dell’Università e della Ricerca (MUR), funded by the European Union – NextGenerationEU.

Appendix A. Validation for Coriolis

To most accurately represent an ABL with an attached wind veer, the terms within Eq. (1) were deemed most appropriate for representing the Coriolis effect and for handling the Ekman spiral via a PI controller. This code modification was validated by comparison with the results

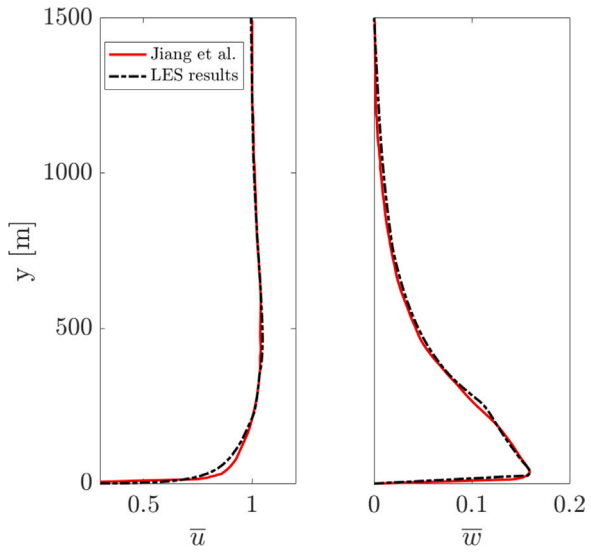

Fig. A.1. Validation of the Coriolis forcing through comparison with Ref. [49]. The curve obtained from the present code is the dash-dotted black line, whereas the red one is the A3 curve of Fig. 3 of the above-mentioned paper.

presented in [49] and is illustrated in Fig. A.1. A comparison of the results showed that there is no appreciable difference between the results of the reference paper and those obtained from the in-house code.

Appendix B. Supplementary data

Within the supplementary material, two videos are included, one for each case under investigation (without and with the Coriolis effect), showing the evolution of the wake by the Q-criterion colored by the streamwise velocity. For each video, we provide first a visualization of the wake flow as produced by LES and three reconstructed flow fields constructed using a decreasing number of modes.

Supplementary material related to this article can be found online at https://doi.org/10.1016/j.ecmx.2024.100830.

Data availability

Data will be made available on request.

References

[1] IRENA. COP28, IRENA and GRA (2023) tripling renewable power and doubling energy efficiency by 2030: crucial steps towards 1.5 °C. Technical report, International Renewable Energy Agency; 2023, 978-92-9260-555-1.
[2] IRENA. IRENA (2019) Future of wind: Deployment, investment, technology, grid integration and socio-economic aspects (A Global Energy Transformation paper). Technical report, Abu Dhabi: International Renewable Energy Agency; 2019, 978-92-9260-155-3.
[3] von Krauland A, Long Q, Enevoldsen P, Jacobson MZ. United States offshore wind energy atlas: availability, potential, and economic insights based on wind speeds at different altitudes and thresholds and policy-informed exclusions. Energy Convers Manage: X 2023;20:100410. http://dx.doi.org/10.1016/j.ecmx.2023.100410.
[4] Kleusberg E, Bernard S, Henningson DS. Tip-vortex breakdown of wind turbines subject to shear. Wind Energy 2019;22:1789–99. http://dx.doi.org/10.1002/we.2403.
[5] Stevens RJ, Meneveau C. Flow structure and turbulence in wind farms. Annu Rev Fluid Mech 2017;49(1):311–39. http://dx.doi.org/10.1146/annurev-fluid-010816-060206.
[6] Troldborg N, Sørensen JN, Mikkelsen RF. Actuator line simulation of wake of wind turbine operating in turbulent inflow. J Phys Conf Ser 2007;75:012063. http://dx.doi.org/10.1088/1742-6596/75/1/012063.
[7] Chamorro LP, Porté-Agel F. Effects of thermal stability and incoming boundary-layer flow characteristics on wind-turbine wakes: a wind-tunnel study. Bound-layer Meteorol 2010;136:515–33. http://dx.doi.org/10.1007/s10546-010-9512-.
[8] Medici D, Alfredsson P. Measurements on a wind turbine wake: 3D effects and bluff body vortex shedding. Wind Energy 2006;9(3):219–36. http://dx.doi.org/10.1002/we.156.
[9] Gambuzza S, Ganapathisubramani B. The influence of free stream turbulence on the development of a wind turbine wake. J Fluid Mech 2023;963:A19. http://dx.doi.org/10.1017/jfm.2023.302.
[10] De Cillis G, Cherubini S, Semeraro O, Leonardi S, De Palma P. The influence of incoming turbulence on the dynamic modes of an NREL-5MW wind turbine wake. Renew Energy 2022;183:601–16. http://dx.doi.org/10.1016/j.renene.2021.11.037.
[11] Gadde SN, Stevens RJ. Effect of coriolis force on a wind farm wake. J Phys: Conf Ser 2019;1256:012026. http://dx.doi.org/10.1088/1742-6596/1256/1/012026.
[12] Abkar M, Porté-Agel F. Influence of the coriolis force on the structure and evolution of wind turbine wakes. Phys Rev Fluids 2016;1:063701. http://dx.doi.org/10.1103/PhysRevFluids.1.063701.
[13] Abkar M, Sørensen JN, Porté-Agel F. An analytical model for the effect of vertical wind veer on wind turbine wakes. Energies 2018;11(7):1838. http://dx.doi.org/10.3390/en11071838.
[14] Howland MF, González CM, Martínez JJP, Quesada JB, Larranaga FP, Yadav NK, Chawla JS, Dabiri JO. Influence of atmospheric conditions on the power production of utility-scale wind turbines in yaw misalignment. J Renew Sustain Energy 2020;12:063307. http://dx.doi.org/10.1063/5.0023746.
[15] Narasimhan G, Gayme DF, Meneveau C. Effects of wind veer on a yawed wind turbine wake in atmospheric boundary layer flow. Phys Rev Fluids 2022;7(11):114609. http://dx.doi.org/10.1103/PhysRevFluids.7.114609.
[16] Porté-Agel F, Bastankhah M, Shamsoddin S. Wind-turbine and wind-farm flows: a review. Bound-Layer Meteorol 2020;1–59. http://dx.doi.org/10.1007/s10546-019-00473-0.
[17] Hoxha B, Shesho IK, Filkoski RV. Optimization of wind farm layout to maximize the energy yield. Energy Convers Manage: X 2024;24:100700. http://dx.doi.org/10.1016/j.ecmx.2024.100700.
[18] Sirovich L. Turbulence and the dynamics of coherent structures. I. Coherent structures. Q Appl Math 1987;45(3):561–71. http://dx.doi.org/10.1090/qam/910462.
[19] Schmid PJ. Dynamic mode decomposition of numerical and experimental data. J Fluid Mech 2010;656:5–28. http://dx.doi.org/10.1017/S0022112010001217.
[20] VerHulst C, Meneveau C. Large eddy simulation study of the kinetic energy entrainment by energetic turbulent flow structures in large wind farms. Phys Fluids 2014;26(2). http://dx.doi.org/10.1063/1.4865755.
[21] Hamilton N, Tutkun M, Cal RB. Wind turbine boundary layer arrays for Cartesian and staggered configurations: Part II, low-dimensional representations via the proper orthogonal decomposition. Wind Energy 2015;18(2):297–315. http://dx.doi.org/10.1002/we.1697.
[22] De Cillis G, Cherubini S, Semeraro O, Leonardi S, De Palma P. POD-based analysis of a wind turbine wake under the influence of tower and nacelle. Wind Energy 2021;24(6):609–33. http://dx.doi.org/10.1002/we.2592.
[23] Debnath M, Santoni C, Leonardi S, Iungo GV. Towards reduced order modelling for predicting the dynamics of coherent vorticity structures within wind turbine wakes. Phil Trans R Soc A 2017;375. http://dx.doi.org/10.1098/rsta.2016.0108.
[24] Jovanović MR, Schmid PJ, Nichols JW. Sparsity-promoting dynamic mode decomposition. Phys Fluids 2014;26(2). http://dx.doi.org/10.48550/arXiv.1309.4165.
[25] Rowley CW, Mezić I, Bagheri S, Schlatter P, Henningson DS. Spectral analysis of nonlinear flows. J Fluid Mech 2009;641:115–27. http://dx.doi.org/10.1017/S0022112009992059.
[26] Sun C, Tian T, Zhu X, Hua O, Du Z. Investigation of the near wake of a horizontal-axis wind turbine model by dynamic mode decomposition. Energy 2021;227:120418. http://dx.doi.org/10.1016/j.energy.2021.120418.
[27] Iungo GV, Santoni-Ortiz C, Abkar M, Porté-Agel F, Rotea MA, Leonardi S. Data-driven reduced order model for prediction of wind turbine wakes. J Phys Conf Ser 2015;625:012009. http://dx.doi.org/10.1088/1742-6596/625/1/012009.
[28] De Cillis G, Semeraro O, Leonardi S, De Palma P, Cherubini S. Dynamic-mode-decomposition of the Wake of the NREL-5MW Wind Turbine Impinged by a Laminar Inflow. Renew Energy 2022;199:1–10. http://dx.doi.org/10.1016/j.renene.2022.08.113.
[29] Jonkman J, Butterfield S, Musial W, Scott G. Definition of a 5-MW reference wind turbine for offshore system development. Golden, CO (United States): National Renewable Energy Lab.(NREL); 2009, http://dx.doi.org/10.2172/947422.
[30] Smagorinsky J. General circulation experiments with the primitive equations: I. The basic experiment. Mon Weather Rev 1963;91(3):99–164.
[31] Martínez-Tossas LA, Churchfield MJ, Leonardi S. Large eddy simulations of the flow past wind turbines: actuator line and disk modeling. Wind Energy 2015;18(6):1047–60. http://dx.doi.org/10.1002/we.1747.
[32] Ciri U, Salvetti M, Carrasquillo K, Santoni C, Iungo G, Leonardi S. Effects of the subgrid-scale modeling in the large-eddy simulations of wind turbines. In: Direct and large-eddy simulation x. Springer; 2018, p. 109–15. http://dx.doi.org/10.1007/978-3-319-63212-4_13.

[33] Ciri U, Petrolo G, Salvetti M, Leonardi S. Large-eddy simulations of two in-line turbines in a wind tunnel with different inflow conditions. Energies 2017;10(6):821. http://dx.doi.org/10.3390/en10060821.
[34] Krogstad På, Eriksen PE. "Blind test" calculations of the performance and wake development for a model wind turbine. Renew Energy 2013;50:325–33. http://dx.doi.org/10.1016/j.renene.2012.06.044.
[35] Sarlak H, Meneveau C, Sørensen JN. Role of subgrid-scale modeling in large eddy simulation of wind turbine wake interactions. Renew Energy 2015;77:386–99. http://dx.doi.org/10.1016/j.renene.2014.12.036.
[36] Santoni C, Ciri U, Rotea M, Leonardi S. Development of a high fidelity CFD code for wind farm control. In: 2015 American control conference. IEEE; 2015, p. 1715–20. http://dx.doi.org/10.1109/ACC.2015.7170980.
[37] Martinez L, Leonardi S, Churchfield M, Moriarty P. A comparison of actuator disk and actuator line wind turbine models and best practices for their use. In: 50th AIAA aerospace sciences meeting including the new horizons forum and aerospace exposition. 2012, p. 900. http://dx.doi.org/10.2514/6.2012-900.
[38] Santoni C, Carrasquillo K, Arenas-Navarro I, Leonardi S. Effect of tower and nacelle on the flow past a wind turbine. Wind Energy 2017;20(12):1927–39. http://dx.doi.org/10.1002/we.2130.
[39] Orlandi P. Fluid flow phenomena: a numerical toolkit, vol. 55, Springer Science & Business Media; 2000, http://dx.doi.org/10.1023/A:1010397420189.
[40] Sørensen JN, Shen WZ. Computation of wind turbine wakes using combined Navier-Stokes/actuator-line methodology. In: 1999 European wind energy conference. Routledge; 2014, p. 156–9. http://dx.doi.org/10.1098/rsta.2014.0071.
[41] Orlandi P, Leonardi S. DNS of turbulent channel flow with two-and three-dimensional roughness. J Turbul 2006;(7):N73. http://dx.doi.org/10.1080/14685240600827526.
[42] Hansen KS, Barthelmie RJ, Jensen LE, Sommer A. The impact of turbulence intensity and atmospheric stability on power deficits due to wind turbine wakes at Horns Rev wind farm. Wind Energy 2012;15(1):183–96. http://dx.doi.org/10.1002/we.512.
[43] Wu Y, Porté-Agel F. Atmospheric turbulence effects on wind-turbine wakes: An LES study. Energies 2012;5(12):5340–62. http://dx.doi.org/10.3390/en5125340.
[44] Talavera M, Shu F. Experimental study of turbulence intensity influence on wind turbine performance and wake recovery in a low-speed wind tunnel. Renew Energy 2017;109:363–71. http://dx.doi.org/10.3390/en5125340.
[45] Cal RB, Lebrón J, Castillo L, Kang HS, Meneveau C. Experimental study of the horizontally averaged flow structure in a model wind-turbine array boundary layer. J Renew Sustain Energy 2010;2(1). http://dx.doi.org/10.1063/1.3289735.
[46] Ekman VW. On the influence of the earth's rotation on ocean-currents. Almqvist & Wiksells Boktryckeri, A.-B.; 1905.
[47] Sescu A, Meneveau C. A control algorithm for statistically stationary large eddy simulations of thermally stratified boundary layers. Q J R Meteorol Soc 2014;140(683):2017–22. http://dx.doi.org/10.1002/qj.2266.
[48] Orlanski I. A simple boundary condition for unbounded hyperbolic flows. J Comput Phys 1976;21(3):251–69. http://dx.doi.org/10.1016/0021-9991(76)90023-1.
[49] Jiang Q, Wang S, Sullivan P. Large-eddy simulation study of log laws in a neutral Ekman boundary layer. J Atmos Sci 2018;75(6):1873–89. http://dx.doi.org/10.1175/JAS-D-17-0153.1.
[50] Hwang Y. Statistical structure of self-sustaining attached eddies in turbulent channel flow. J Fluid Mech 2015;767:254–89. http://dx.doi.org/10.1017/jfm.2015.24.
[51] Kovasznay LS, Kibens V, Blackwelder RF. Large-scale motion in the intermittent region of a turbulent boundary layer. J Fluid Mech 1970;41(2):283–325. http://dx.doi.org/10.1017/S0022112070000629.
[52] Abkar M, Porté-Agel F. Influence of atmospheric stability on wind-turbine wakes: a large eddy simulation study. Phys Fluids 2015;27(3). http://dx.doi.org/10.1063/1.4913695.
[53] Mao X, Sørensen JN. Far-wake meandering induced by atmospheric eddies in flow past a wind turbine. J Fluid Mech 2018;846:190–209. http://dx.doi.org/10.1017/jfm.2018.275.
[54] Gupta V, Wan M. Low-order modelling of wake meandering behind turbines. J Fluid Mech 2019;877:534–60. http://dx.doi.org/10.1017/jfm.2019.619.